CrossMark

J. Plasma Phys. (2021), *vol*. 87, 855870202 © The Author(s), 2021.
Published by Cambridge University Press
doi:10.1017/S0022377821000234

A fast tool for ICRH+NBI modelling within the EU-IM framework

Dirk Van Eester [1],†, E.A. Lerche[1], Ph. Huynh[2], T. Johnson [3], JET contributors[4] and EUROfusion-IM team[5]

[1]LPP-ERM/KMS, EUROfusion Consortium Member - Trilateral Euregio Cluster, Brussels, Belgium

[2]CEA, IRFM, F-13108 Saint-Paul-lez-Durance, France

[3]Dept. of Fusion Plasma Physics, School of Electrical Engineering and Computer Science, KTH, Stockholm, Sweden

[4]See the author list of E. Joffrin et al., *Nucl. Fusion* **59** (2019) 112021

[5]See http://www.euro-fusionscipub.org/eu-im

(Received 2 November 2020; revised 22 February 2021; accepted 23 February 2021)

Most if not all tokamak heating scenarios involve multiple ion populations being heated simultaneously. To allow the simulation of various aspects of physics dynamics determining the characteristics of operational scenarios in a flexible way, speedy yet sufficiently accurate models are needed, and they should be connected to each other via a 'backbone'. Under the umbrella of EUROfusion's Integrated Modelling efforts, such a structure is provided. The present paper focuses on one physics aspect: auxiliary heating. After solving the wave equation or beam source equation, this requires solving a set of coupled Fokker–Planck equations for the various populations involved. The adopted modules – enabling accounting for the Coulomb collisional interaction of several non-Maxwellian (minority, majority and beam) populations – are discussed and a practical example of their use is provided: the JET 'baseline' scenario heating a minority of ^{3}He ions in a balanced D+T mix heated by D and T neutral beams.

Key words: plasma simulation, fusion plasma, plasma heating

1. Introduction

The plasma dynamics in fusion machines is extremely complex in view of the fact that a hot, magnetised plasma away from thermal equilibrium has many degrees of freedom. Up to a point, the evolution of any physical quantity is influenced by any other quantity. For that reason, theory/modelling and experiments of fusion-relevant scenarios always go hand in hand. Experimental evidence allows us to identify the key parameters to be withheld in models (computational models would need to run for a prohibitively long time when trying to capture all individual aspects of the dynamics of charged particles, and hence theoretical models necessarily need to make many assumptions to produce results in a reasonable time) while modelling provides deeper insight into the plasma fate and allows us to venture forward along possible experimental roads.

† Email address for correspondence: d.van.eester@fz-juelich.de

https://doi.org/10.1017/S0022377821000234 Published online by Cambridge University Press

It is impossible to cast all aspects of the physics into a single 'master equation'. But bringing together the description of various subaspects can be done by connecting them via a 'backbone', all numerical codes reading from the same shared and standardised database at the outset of a computation and feeding back output to it. The EUROfusion Integrated Modelling and Analysis Suite (IMAS) offers such a framework (Imbeaux *et al.* 2010; Pinches *et al.* 2018; Romanelli *et al.* 2020). Much like experimental data from actual experiments, the database consists of a number of 'shots' and users can load the parameters needed in their specific code at specific times of interest. A dedicated team ensures the backbone is maintained, and contributors, external to the basic team, make their codes conform to the backbone to allow their codes to run in a bigger 'workflow'. Available codes are compiled as 'actors' and can be linked together in a flexible way via a 'Kepler' graphical user interface (The Kepler Project 2008) or, more directly, via a Python wrapper (Schneider *et al.* 2017). More importantly, the common input and output structure allows us to interchange codes which look into a specific aspect of the physics with other similar ones. On the one hand this is useful for cross-checking that codes based on the same physics indeed produce compatible results. But on the other hand, this allows specific codes to be used when modelling scenarios that require special attention. This kind of 'plug-in/plug-out' philosophy allows for very flexible testing and modelling. The integrated modelling efforts started a decade ago (Imbeaux *et al.* 2010; Strand *et al.* 2010) and the backbone has now reached a level that massive exploitation has become possible. The EUROfusion's Integrated Modelling (EU-IM) framework is routinely applied for modelling present-day machines such as JET, as well as future test devices such as ITER and DEMO (Falchetto *et al.* 2014; Imbeaux *et al.* 2015; Falchetto *et al.* 2016; Pinches *et al.* 2018; Strand *et al.* 2018; Voitsekhovitch *et al.* 2018; Falchetto *et al.* 2019; Romanelli *et al.* 2019, 2020). Likely the biggest application of the EU-IM framework efforts is the European Transport Solver (ETS) (Coster *et al.* 2010; Kalupin *et al.* 2012). It contains equilibrium solvers, auxiliary heating modules, magnetohydrodynamics (MHD) simulators and (core as well as edge edge) transport equation solvers; a qualitative sketch based on (Coster *et al.* 2010) is depicted in figure 1. The transport codes require particle and energy source input. A variety of electron cyclotron resonance heating (ECRH) and ion cyclotron resonance heating (ICRH) codes, as well as neutral beam solvers is available; see for example Huynh *et al.* (2019) for an application of the ICRH+NBI heating modules in ETS focused on JET and Schneider *et al.* (2017, 2019, 2020) for ITER applications. To account for the birth of fusion-born populations and to compute accurate estimates of the neutron production in deuteron–tritium (D–T) plasmas, data banks of nuclear cross-sections are interfaced with ETS (Coster *et al.* 2010). Although some EU-IM modules describe specific physics aspects in fair detail and require non-negligible CPU time, the modules most frequently used aim at swiftly providing approximate answers while allowing many aspects of importance to be accounted for simultaneously and, up to a point, self-consistently. In that sense, the EU-IM framework can be considered as complementary to high-level detailed numerical codes addressing a specific aspect of magnetic confinement fusion related physics in detail.

The present paper (associated with a talk that was delivered at the Ghent 2019 European Fusion Theory Conference) reports on recent upgrades in some of the Fokker–Planck tools routinely used under the IMAS umbrella to model ICRH or radio frequency (RF) heating. These tools were specifically designed to model scenarios that simultaneously heat various species and that combine wave with neutral beam injection heating, so that the interplay of various minority as well as majority non-Maxwellian populations needs to be accounted for when computing the power source terms to be passed on to the transport equation. This requires a change in philosophy with respect to what is commonly done when solving

https://doi.org/10.1017/S0022377821000234 Published online by Cambridge University Press

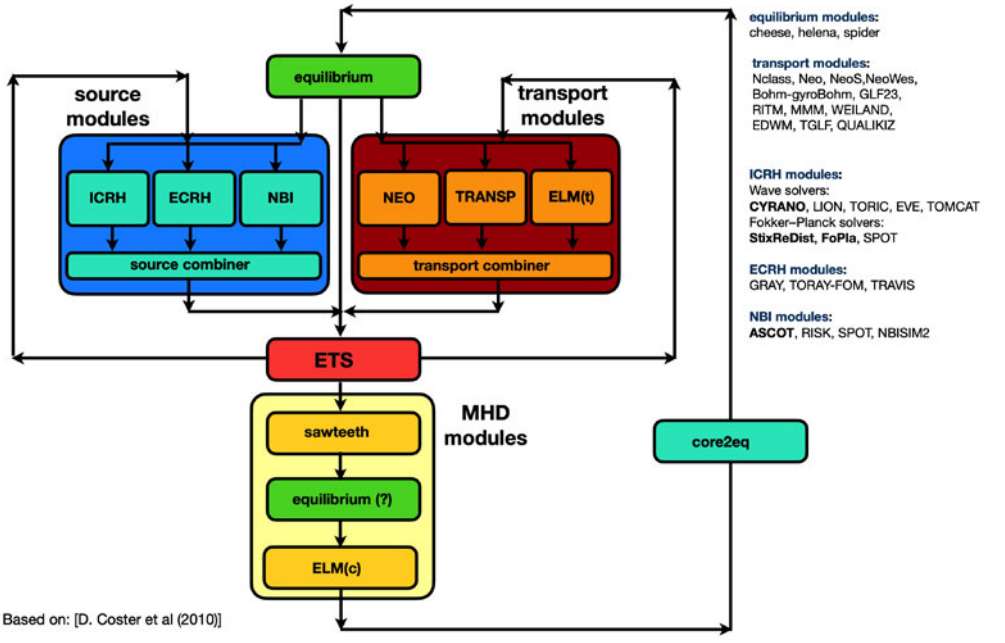


FIGURE 1. Qualitative sketch of the workflow in which the ETS is run.

the Fokker–Planck equation on a series of magnetic surfaces: the fact that the collision operator is conservative, so that the net sum of all collisional interactions needs to be zero, requires an energy loss term to be included in the Fokker–Planck equation of each of the types of species, independent of whether beam or wave heating is applied. The paper is organised as follows. After the present introduction, some general remarks on ICRH modelling will be provided (§ 2). A suitably simplified form of the Fokker–Planck equation for numerical models is provided in § 3. In § 4 the Fokker–Planck equation is revisited and presented in a different form that allows for faster numerical solving. Some numerical issues that arise when solving the Fokker–Planck are listed in § 5. Section 6 is devoted to the discussion of solving coupled Fokker–Planck equations and the need for the implementation of losses. In a brief section (§ 7) the adopted procedure for computing the neutron rate for arbitrary distributions is provided. Section 8 provides a practical example illustrating the modelling of combined ICRH and neutral beam injection (NBI) heating involving directly heated minorities, majorities as well as beam populations in one of the JET–ILW scenarios expected to be exploited in the upcoming D–T campaign. After that, conclusions are drawn. Two appendices provide information on some numerical tools used: one focuses on the finite element approach and one on the influence matrix method.

2. General remarks on ICRH modelling

Ion cyclotron resonance heating involves processes occurring on very different time scales. The most rapid time scale is that of the RF dynamics. Since the RF frequency is in the MHz range, all variations of the background against which these effects occur can safely be neglected. For that reason the wave equation is typically solved as a driven problem, assuming the densities and temperatures of the background species are known and prescribed. Power transferred from the waves to the particles is further redistributed among the plasma constituents through Coulomb collisional interaction.

https://doi.org/10.1017/S0022377821000234 Published online by Cambridge University Press

This process – happening on time scales that are a few orders of magnitude larger than the RF time scale – is described by the Fokker–Planck equation. Energy and particle transport across magnetic surfaces is commonly assumed to occur on time scales that are longer than those on which slowing down processes occur. When this is not the case, the Fokker–Planck equation needs to be solved accounting for temporal evolution of the distribution functions. Solving the wave equation yields the RF perturbed electric field, while solving the Fokker–Planck equation allows us to determine the slowly varying distribution function F_o. Provided the wave–particle interaction is modelled self-consistently, the power density as seen by the wave equation is identical to that of the Fokker–Planck equation,

$$P_{\rm abs} = \frac{\partial}{\partial t}\left[\int {\rm d}\boldsymbol{v}\,{\rm d}\boldsymbol{x}\epsilon F_o\right] = \left[\int {\rm d}\boldsymbol{v}\,{\rm d}\boldsymbol{x}\epsilon\,\left.\frac{\partial F_o}{\partial t}\right|_{\rm RF}\right] = \frac{1}{2}Re\left[\int {\rm d}\boldsymbol{v}\,{\rm d}\boldsymbol{x}\epsilon Q(F_o)\right]$$
$$= \frac{1}{2}Re\left[\int {\rm d}\boldsymbol{v}\,{\rm d}\boldsymbol{x}\frac{q}{m}[\boldsymbol{E}+\boldsymbol{v}\times\boldsymbol{B}]^*.[\nabla_{\boldsymbol{v}}\epsilon]f_{\rm RF}\right] = \frac{q}{2}Re\left[\int {\rm d}\boldsymbol{v}\,{\rm d}\boldsymbol{x}\boldsymbol{E}.\boldsymbol{J}_{\rm RF}\right], \qquad (2.1)$$

in which Q is the RF quasilinear diffusion operator needed in the Fokker–Planck equation,

$$Q(F_o) = \nabla_{\boldsymbol{v}}.\left[\frac{q}{m}[\boldsymbol{E}+\boldsymbol{v}\times\boldsymbol{B}]^*\int_{-\infty}^{t}{\rm d}t'\frac{q}{m}[\boldsymbol{E}+\boldsymbol{v}\times\boldsymbol{B}].\nabla_{\boldsymbol{v}}\right]F_o, \qquad (2.2)$$

and $\boldsymbol{J}_{\rm RF} = \int {\rm d}\boldsymbol{v}\boldsymbol{v}f_{\rm RF}$ is the RF perturbed current density needed in the wave equation. Here $f_{\rm RF}$ is the perturbed distribution function,

$$f_{\rm RF} = -\int_{-\infty}^{t}{\rm d}t'\frac{q}{m}[\boldsymbol{E}+\boldsymbol{v}\times\boldsymbol{B}].\nabla_{\boldsymbol{v}}F_o. \qquad (2.3)$$

In the above, ϵ is the energy, q the charge and m the mass of the considered particle population; $\boldsymbol{v}$, $\boldsymbol{E}$ and $\boldsymbol{B}$ are the velocity, the RF electric field and the RF magnetic field, respectively. Although the above identity suggests it is straightforward to ensure a self-consistent description, there is not a single suite of RF codes currently in existence that actually solves this problem generally (i.e. simultaneously accounting for all waves supported by the plasma and for the various arbitrary distribution functions of interacting minorities, majorities and beams) while putting the wave and Fokker–Planck equations on the same footing (i.e. using fully self-consistent expressions in the wave's dielectric response and the quasilinear diffusion operator). In practice, the wave and Fokker–Planck equations are solved making somewhat differing approximations, allowing a much more speedy description, while retaining the dominant physics. From the wave equation point of view the main simplification is that the dielectric response assumes the electric field varies slowly during a Larmor gyration – yielding a truncation (commonly to second order) in terms of finite Larmor radius corrections. From the Fokker–Planck point of view all finite Larmor radius effects are typically accounted for, but the electric field is assumed to only have a single perpendicular wave component mode, i.e. the homogeneous plasma response is assumed to capture the main dynamics although the dielectric response is actually a differential or integro–differential operator. A set of codes coming very close to self-consistency is the AORSA/CQL3D pair of solvers (Harvey *et al.* 1992; Jaeger *et al.* 2006; Petrov & Harvey 2016) accounting for all finite Larmor radius corrections but considering a locally homogeneous RF diffusion operator, and very recent work by Lee *et al.* (2017) where, oppositely, only up to second-order finite Larmor radius

https://doi.org/10.1017/S0022377821000234 Published online by Cambridge University Press

correction terms are retained, but the wave diffusion operator is a differential operator in full agreement with the expansion used in the TORIC code.

All wave and Fokker–Planck codes installed in EU-IM make assumptions, some codes making more drastic simplifications than others. A common assumption is that guiding centres are glued to magnetic surfaces allowing us to study the dynamics of the collisional interaction of charged populations sharing a magnetic surface separate from transport processes radially across surfaces.

Making approximations to cut down on computer time necessarily comes at a price. The fact that the wave and Fokker–Planck equation are not derived making the same assumptions excludes the description of being truly self-consistent. Rather than matching the actual electric fields at the exact point of resonance, the wave and Fokker–Planck descriptions match the local power densities on each of the considered magnetic surfaces. Since the distribution function is a complicated (and for the case of cyclotron harmonic heating a very sensitive) function of the input power, this requires iteratively solving the Fokker–Planck equation on an appropriate (non-uniform) velocity grid covering an energy range, allowing us to capture the formation of high-energy tails as well as the slowing down and thermal ion populations until the proper rescaling factor is found, while freezing the wave polarisation and perpendicular wavenumber. A crude estimate of the maximal energy to be included is provided by locating the first zero of the RF diffusion coefficient (which acts as a barrier beyond which the distribution function drops significantly), typically in the range of a few MeV. If treating the problem fully self-consistently were possible this iteration procedure would be unnecessary and the electric field at the resonance could simply be adopted directly, the various Fokker–Planck equations being solved as an initial value, i.e. time stepping problem.

In the present work the focus is on fast and hence simple methods to model tokamak plasma heating scenarios in which various ion populations are simultaneously heated and the Coulomb collisional interaction of multiple non-Maxwellian (minority, majority and beam) populations is crucial. It is complementary to highly sophisticated but CPU time consuming solvers capable of providing a more detailed description of many aspects. Now AORSA is already routinely coupled with the CQL3D 3-D Fokker–Planck solver (Harvey *et al.* 1992; Jaeger *et al.* 2006; Petrov & Harvey 2016), the EVE code is run together with the Monte Carlo code SPOT (Schneider *et al.* 2016; Joly *et al.* 2019), TORIC is routinely used in conjunction with SSFPQL (Brambilla 1994; Bilato *et al.* 2011) as well as CQL3D (see for example Lee *et al.* 2017) and the CYRANO wave code (Lamalle 1994) was coupled to the BATCH Fokker–Planck code (Van Eester 2001) when describing RF heating of a D beam at the fundamental cyclotron frequency (Lerche *et al.* 2009). The Monte Carlo test-particle approach is increasingly popular since it allows a very intuitive insight by actually tracing a large number of orbits. Aside from the earlier mentioned SPOT, examples are ASCOT (Hirvijoki *et al.* 2014), SELFO (Hedin *et al.* 2002) and SCENIC (Jucker 2010).

3. A suitable one-dimensional form of the Fokker–Planck equation

When magnetic surfaces are decoupled from each other except for transport terms mocked up by a local loss term (see the discussion later), a suitably simplified steady-state form of the one-dimensional (1-D) Fokker–Planck equation for distributions only depending on the velocity is (Karney 1986)

$$\frac{1}{v^2}\frac{\partial}{\partial v}\left[v^2\left(A\frac{\partial F_o}{\partial v}+BF_o\right)\right]+S-\frac{F_o}{\tau_P}=0 \tag{3.1}$$

https://doi.org/10.1017/S0022377821000234 Published online by Cambridge University Press

where A has an RF and a collisional contribution ($A = A_{\rm RF} + D_{vv,\rm coll}$) where

$$A_{\rm RF} = K_{\rm RF} \left| J_{N-1} + \frac{E_-}{E_+} J_{N+1} + J_N \frac{E_{//}}{E_+} \right|^2 , \tag{3.2}$$

while $B = B_{\rm coll} + B_{\rm loss}$ has a collisional term ($B_{\rm coll} = -F_{v,\rm coll}$) and a loss term

$$B_{\rm loss} = \frac{v}{2} \left[\frac{1}{\tau_E} - \frac{1}{\tau_P} \right]; \tag{3.3}$$

τ_E is the energy loss time and τ_P the particle loss time. The wave polarisations of the RF electric field (E_+ is the electric field component rotating in the sense of the ions, E_- rotates in the sense of the electrons and $E_{//}$ is the parallel electric field) are evaluated solving the wave equation.

The reason for only solving the time-independent solution is twofold. (1) It allows a rigorous check on energy conservation. Especially when the interaction of many populations needs to be tracked, energy conservation is a highly desirable asset. (2) It provides the desired solution faster. Solving the time-dependent Fokker–Planck equation showed that the setting up of the final distribution function happens in three characteristic times when all species distributions are allowed to be modified: (i) the direct impact of the RF waves (yielding a much faster response in the case of second harmonic heating than in the case of fundamental heating); (ii) the formation of the distribution under the influence of Coulomb collisions crudely in equilibrium for the ions; (iii) the formation of the distribution under the influence of Coulomb collisions in equilibrium both with the other ions and electrons. To enable simulations of full discharges, the speed of computation is deemed crucial in EU-IM, in spite of the fact that it requires sacrificing certain physics aspect details. Since EU-IM allows for time stepping, time-dependent solving of the Fokker–Planck equation is to be implemented at some future stage, however.

Note that only the relative polarisations appear in the above. Per magnetic surface and per specie, the constant $K_{\rm RF}$ is adjusted to ensure the RF power density corresponding to the distribution obtained solving the Fokker–Planck equation is the externally imposed RF power density. The above Fokker–Planck equation is a simplified version of the full 3-D equation that ought to be solved. It ignores pitch angle effects and does not properly model (neoclassical collision as well as RF induced) radial diffusion across magnetic surfaces. Because of these simplifications, solving the equation is fast, making it a suitable tool for implementation in the ETS. For more detailed analysis of specific aspects related to for example particle trapping, this tool is too crude and more complete models need to be considered. The coefficients of the collision operator are sums on the contributions from each of the background species b influencing the test species a, e.g. $F_{v,\rm coll} = \sum_b F_v^{a/b}$.

When the background distribution is Maxwellian, the collision operator coefficients are

$$D_{vv}^{a/b} = \frac{\Gamma^{a/b}}{2v} \left[\frac{\epsilon(u) - u\epsilon'(u)}{u^2} \right], \tag{3.4}$$

$$F_v^{a/b} = -\frac{\Gamma^{a/b}}{v^2} \frac{m_a}{m_b} \left[\epsilon(u) - u\epsilon'(u) \right], \tag{3.5}$$

in which $u = v/2^{1/2} v_t$ (v_t is the thermal velocity) and ϵ is the error function. The constant $\Gamma^{a/b}$ is

$$\Gamma^{a/b} = \frac{N_b q_a^2 q_b^2 ln\Lambda^{a/b}}{4\pi\epsilon_o^2 m_a^2} \tag{3.6}$$

https://doi.org/10.1017/S0022377821000234 Published online by Cambridge University Press

in which $\ln \Lambda$ is the Coulomb logarithm. For a general distribution, these expressions generalise to

$$D_{vv}^{a/b} = \frac{4\pi\Gamma^{a/b}}{3N_b}\left[\frac{1}{v^3}\int_0^v \mathrm{d}pp^4 F_{o,b}(p) + \int_v^\infty \mathrm{d}ppF_{o,b}(p)\right], \tag{3.7}$$

$$F_v^{a/b} = -\frac{4\pi\Gamma^{a/b}}{N_b}\frac{m_a}{m_b v^2}\int_0^v \mathrm{d}pp^2 F_{o,b}(p). \tag{3.8}$$

The total D_{vv} and F_v are the sum over the various species b for a test species a, the corresponding masses are $m_{...}$ and $N_{...}$ the corresponding densities.

The adopted source is the broadened delta function $\delta(v_o - v)$ where v_o is the birth velocity. The smooth version $\exp[-([v - v_o]/\Delta_S)^2]/[v^2\pi^{1/2}\Delta_S]$ rather than the delta function itself is used to avoid breaks in the distribution's derivatives which may give rise to numerical issues when introducing the obtained distribution function into other EU-IM modules.

As the RF term nor the (non-simplified) collision term create or annihilate particles one readily finds that $\langle S\rangle = N_a/\tau_P$ where $\langle M(v)\rangle = 4\pi\int_0^\infty \mathrm{d}vv^2 M(v)$. Similarly $\langle L(F_o)mv^2/2\rangle = -E_{\mathrm{tot}}/\tau_E$ in which E_{tot} is the total energy and $L(F_o) = L_E + L_P$ with

$$L_E(F_o) = \frac{1}{v^2}\frac{\partial}{\partial v}\left[\frac{v^3}{2}\left(\frac{1}{\tau_E} - \frac{1}{\tau_P}\right)F_o\right], \tag{3.9}$$

$$L_P(F_o) = -\frac{F_o}{\tau_P}. \tag{3.10}$$

The incoming wave plus neutral beam power density is balanced by the collisional and non-collisional losses.

Unlike the Stix approach which allows integrating the Fokker–Planck equation for non-beam populations rapidly as a first-order differential equation using a simple semianalytical expression (see later), accounting for beam sources necessitates solving the actual second-order differential equation. Imposing vanishing outgoing flux both at $v = 0$ and $v = \infty$ constitutes a logical set of boundary conditions which defines the unique solution compatible with a given source. Since boundary conditions need to be imposed at either end of the integration domain and in view of the fact that the distribution becomes very small at high energy, shooting methods are commonly ill-suited to solving the equation and a more global method is required. The finite element method is robust, but somewhat memory as well as time consuming. Some details of its practical implementation exploiting suitable third-order base functions allowing us to directly obtain F_o and $\mathrm{d}F_o/\mathrm{d}v$ upon solving the linear system associated with the variational formulation of the differential equation are provided in appendix A.

It goes without saying that a 1-D isotropic distribution function does not capture all details of the actual 5*D* distributions. Effects such as particle trapping and RF induced neoclassical radial diffusion are not included. Moreover, it is known that RF heating mainly affects the perpendicular energy while leaving the parallel energy roughly untouched. The present tool is suitable for a fast evaluation of sets of interacting distributions and assessing the importance of this effect. The best known example of its use is the identification and qualitative description of synergistic effects: heating a tokamak plasma using beams as well as waves achieves a heating efficiency superior to the efficiency obtained as the sum of the two heating mechanisms apart. The basic reason for this synergy is that beam 'preheating' cranks up the temperature of the thermal bulk

https://doi.org/10.1017/S0022377821000234 Published online by Cambridge University Press

populations and makes the plasma less collisional. The simple picture of this phenomenon is that steady state of the energy level locally requires the balance of incoming energies and (Coulomb collisionally) lost energies. Reducing the friction allows for reaching higher energies for a given RF power level than is the case in the absence of beam 'preheating'. In particular for harmonic heating, there is equally a second effect: as harmonic heating is only potent at higher energy, neutral beam injection provides a seed of already energetic particles on which the waves can act more efficiently. There is also an obvious beneficial synergistic effect of RF heating on beam populations: upon Coulomb collisionally slowing down, RF induced high-energy tails transfer a non-negligible fraction of their power to the electrons. As a consequence the electron temperature increases, which increases the critical velocity. This allows more of the beam power to flow to the ions, causing the bulk ion temperature to rise which in turn enhances the fusion rate.

In defence of the here discussed simple model adopted in ETS, it should be remembered that effects such as trapping only become important when a significant variation of the magnetic field strength is felt along particle orbits. When studying auxiliary heating close to the plasma core, trapping can be considered as a secondary effect. Also, the fact that isotropic distributions are considered is less dramatic than it seems at first sight: Stix (1992) showed that the tail energies predicted by a model assuming F_o only depends on the velocity v essentially differ by a factor of $2/3$ from the prediction with a model assuming the parallel velocity is irrelevant and assuming F_o solely depends on the perpendicular velocity component $v_\perp$. Intuitively this makes sense, the incoming energy now needing to be redistributed over only two perpendicular velocities rather than over all three. Comparing two-dimensional (2-D) Fokker–Planck computations with the here adopted 1-D model, one can see that at low RF power densities Coulomb collisions manage to isotropise the distribution so that the approximation $F_o(v)$ is more suitable. At very high RF power densities the 2-D results yield tail energies more closely related to the results obtained assuming $F_o(v_\perp)$. At intermediate power densities the predicted tail energies are in-between the two. So, from a purely pragmatic point of view, one can make a prediction at the nominal power density and repeat it at $3/2$ that density to define the two 'boundaries' of the range of tail energies between which 2-D models would predict the actual tail energy. Hence assuming the distribution only depends on a single velocity component delivers information that is meaningful and does so at low computational cost. But evidently a simple model, by definition, should not be used to formulate definitive answers. It merely is a tool to highlight a possible road.

4. The Fokker–Planck equation revisited

In absence of particle sources and losses, the Fokker–Planck equation can be solved immediately: integrating once yields

$$v^2\left(A\frac{\partial F_o}{\partial v}+BF_o\right)=ct. \tag{4.1}$$

The flux being zero at $v=0$ as well as at $v=\infty$, the integration constant has to be zero. Integrating further yields

$$F_o \propto \exp\left[-\int_0^v \frac{B}{A}\mathrm{d}v\right], \tag{4.2}$$

the remaining integration constant being determined by the fact that the density is prescribed. Up to the minor upgrade that an energy loss has been allowed for and that the solution holds for any background and cyclotron harmonic, the obtained solution

https://doi.org/10.1017/S0022377821000234 Published online by Cambridge University Press

is the well known solution of Stix (1992); this upgrade was extensively discussed in Van Eester & Lerche (2011). Rather than solving the Fokker–Planck equation for a single 'heated' specie, a set of coupled Fokker–Planck equations modelling the fate of the power transferred from the RF waves to various ions is typically solved by the Fokker–Planck model most standardly used in the ETS. The Fokker–Planck module computing the Coulomb collisional redistribution of RF power for the case when the test population has no source is labelled 'StixReDist'.

When there is a particle source, a particle loss term has to be included for a steady-state solution to exist. The Stix procedure can now no longer be used but the reasoning in terms of the flux still holds. Integrating the full equation now yields

$$v^2\left(A\frac{\partial F_o}{\partial v}+BF_o\right)-\frac{1}{\tau_P}\int_0^v \mathrm{d}v v^2F_0+\int_0^v \mathrm{d}v v^2S=ct. \tag{4.3}$$

As for the sourceless case, the integration constant needs to be zero since the net flux from source and loss terms needs to be zero at infinity (the last two terms on the left-hand side need to balance one another since the first two approach zero, F_0 and its derivative vanishing at $v=\infty$). Defining a new dependent variable $Y=\int_0^v \mathrm{d}v v^2F_0$ (Y is the density integral up to the factor 4π arising from the integration over the pitch and gyroangle) and expressing the derivatives of this function in terms of the distribution F_0 and its derivative yields the equation

$$A\frac{\mathrm{d}^2Y}{\mathrm{d}v^2}+\left[-\frac{2A}{v}+B\right]\frac{\mathrm{d}Y}{\mathrm{d}v}-\frac{Y}{\tau_P}+\int_0^v \mathrm{d}v v^2S=0. \tag{4.4}$$

As boundary conditions, we impose that the flux needs to be zero at $v=0$ and $v=\infty$. Filling out the relations $F_0=v^{-2}\,\mathrm{d}Y/\mathrm{d}v$ and $\mathrm{d}F_0/\mathrm{d}v=[v\,\mathrm{d}^2Y/\mathrm{d}v^2-2\,\mathrm{d}Y/\mathrm{d}v]/v^3$, this condition can readily be transformed into the intuitive $Y(v=0)=0$, i.e. density integral at $v=0$ is zero, and $Y(v=\infty)=\tau_P\int_0^\infty \mathrm{d}v v^2S=N_a/[4\pi]$, i.e. the density integral up to $v=\infty$ comprises the whole distribution.

Aside from the 'StixReDist' module needed to solve the Fokker–Planck equation in the absence of particle sources, both versions of the Fokker–Planck equation have been installed in the 'FoPla' Fokker–Planck module of the ETS relevant for beam or fusion α populations and can be used upon properly setting one of the input flags. A number of solvers is also available and can be activated; this is equally done via input flags.

5. Numerical issues when solving coupled Fokker–Planck equations

Both the wave and Fokker–Planck equations are equations that need particular attention to ensure the solution found is accurate. From the wave equation point of view, the difficulty lies in the fact that the plasma admits wave modes of very different wavelengths and that both propagative and evanescent regions occur. For typical parameters in machines such as JET, Bernstein waves are millimetric while the fast wave has a wavelength of a few 10s of centimetres. Both need to be traced, forcing grid densities to be high. Tackling the difficulties of the wave equation falls beyond the scope the present paper. The difficulty of the Fokker–Planck equation lies in the fact that wave heating creates high energy tails, the particle density of which is extremely modest (the distribution functions are often six to eight orders of magnitude smaller in the high energy compared with the thermal region) while they can carry a substantial part of the wave energy. Inaccurately treating the high-energy part of the distribution yields results that at best bear weak resemblance to the actual solution. Back-of-the-envelope computations

https://doi.org/10.1017/S0022377821000234 Published online by Cambridge University Press

show that distributions decay exponentially as a function of energy under the influence of Coulomb collisions, but auxiliary and in particular RF heating subtly but importantly modifies this behaviour. Fundamental cyclotron heating is dominantly active in the thermal region but allows minority tails to reach energies in the MeV range. Because the waves most strongly interact with particles with modest energies in regions where the particle density is high, solving the Fokker–Planck equation for this type of heating usually does not require specific attention on v-gridding unless the power densities are high or the concentration of the population low (minority heating). Harmonic heating, on the other hand, is a more 'touchy' heating scheme since it does not affect the thermal population (except indirectly by fast particles slowing down) but rather accelerates a very small number of already relatively fast particles to even higher energies. Because it affects a very small subpopulation, the response of the distribution function to the power density is highly nonlinear. A modest change of the power density can cause a non-negligible change of the energy density at high energies without dramatically changing the particle distribution itself. Finding suitable forms of the Fokker–Planck equation that allow fast yet accurate integration is therefore a point of attention. For significant RF power densities, the tail commonly stretches up to the first zero of the quasilinear diffusion function containing a combination of Bessel functions (see (3.2)). Beyond this velocity, the distribution drops by several orders of magnitude. Subsequent zeros of the quasilinear diffusion operator are extra barriers through which only an increasingly small number of particles can leak, forming a distribution looking like a staircase when plotting it in log scale. Because of the drop in density when crossing the zeros, the solution is usually well described by choosing $v_{\max}$ somewhat larger than the velocity corresponding to the first zero. Truncating the integration grid at too small $v_{\max}$ and forcing the distribution or the flux to be zero there by imposing the boundary condition that no particle can escape to higher v deceivingly gives the impression of a converged solution, in particular for harmonic heating cases where only a small number of already energetic particles can be accelerated to even higher velocities by the waves.

Solvers guaranteeing a speedier integration of the equations are of great benefit, especially when they are used in a suite of codes such as in the ETS. Many scenarios involve the interaction of various species, all of which undergo Coulomb collisions and therefore interact with each other. Because the set of coupled Fokker–Planck equations needs to be solved on each magnetic surface, and because of the fact that the quasilinear diffusion operator contains the factor K_{RF} that needs to be adjusted to ensure the power density corresponding to the F_os found when solving the Fokker–Planck equation equals the power density found by the wave equation on each magnetic surface, the Fokker–Planck equation has to be solved many thousands of times during a single run. A too slow Fokker–Planck solver makes the tool useless in practice. In the absence of a beam population the Fokker–Planck equation can be solved swiftly and accurately by a brute force semianalytical integration, as was demonstrated by Stix. This advantage is lost when a particle source term is introduced. Because boundary conditions need to be imposed at either end of the velocity interval in which the distribution exists, a global method of integration is needed. Classical methods such as the finite element or finite difference method allow for the recasting of the equation into a system of coupled linear equations that needs to be solved. Inverting the corresponding system matrix is much more time consuming than the interval-by-interval integration required in Stix's Fokker–Planck resolution method. Moreover, storing the system matrix requires significant memory, especially when not exploiting the fact that the system matrix is sparse. Iterative solvers accounting for the sparseness of the system matrix potentially allow us to push down the required computation time. As a check, the conjugate gradient method was explored

https://doi.org/10.1017/S0022377821000234 Published online by Cambridge University Press

alongside the classical Gaussian elimination suitable for full matrices. In spite of requiring a large number (≈1000) of iterations involving matrix–vector multiplications – in which the sparseness is accounted for by storing the matrix in compact form, only keeping the non-zero elements – sparse-matrix solvers outperform the full-matrix solver. It was found, though, that iterative methods are useful to get a first good guess of the solution but that their use is limited in practice since the magnitude of the distribution function differs by many orders of magnitude, making the global error estimates by which 'convergence' is assessed by sparse solvers a poor representative of actual local convergence. A method that allows avoiding the need to invert a big matrix is the influence matrix method. Because this is an interesting while relatively unknown technique, it is described in some detail in appendix B.

6. Coupled Fokker–Planck equations, collisions and losses

The dynamics of the interaction of populations of charged particles in the presence of RF heating sources has many aspects. It is customary to treat these aspects by different equations assuming they appear on different time scales. The fastest time scale is that of the wave oscillation at the frequency of the generator (MHz range; modelled by the wave equation prescribing the driver frequency f, i.e. assuming all perturbed quantities vary as $\exp(-i\omega t)$ with $\omega = 2\pi f$, and allowing us to average over an oscillation cycle when defining the quasilinear diffusion coefficients needed in the Fokker–Planck equation). The slowest time scales describes the slow evolution of macroscopic quantities such as the density and temperature (Hz range; modelled by the transport equations and typically time dependent). In-between these time scales lies the time scale of interest for the Fokker–Planck equation (kHz range for bounce orbit dynamics, allowing a smoothing/averaging over many bounce cycles when composing the input sources for the transport equations). Some of the phenomena described by the Fokker–Planck equation are, however, occurring on time scales not well separated from transport phenomena. To keep the computational time reasonable, the Fokker–Planck equation is typically solved on a set of magnetic surfaces, the implicit reasoning being that orbits do not deviate much from an average radial position. This approach is deemed suitable in the present paper. More sophisticated Fokker–Planck models add another dimension to the description and account for the cross-talk between magnetic surfaces, i.e. the Fokker–Planck equation is solved for the whole plasma volume.

The simplest and most routinely used Fokker–Planck solvers look at the problem of Coulomb collisional slowing down of a single minority population that is heated by waves but has reached a steady state. This is, for example, the approach adopted in the TRANSP code (Hawryluk *et al.* 1980). In that case energy losses are commonly not even considered and the net power balance is straightforward: the incoming wave power is collisionally passed on to the various bulk plasma constituents. Because the minority density is small, the self-collisions are ignored and the linearised version of the collision operator can be used. Moreover, because the minority is the only heated population, the other populations must be close to Maxwellian so that simplified expressions for the collision operator can be exploited. This is qualitatively depicted in figure 2(*a*). The resulting collisional redistribution profile is a source term for solving the energy transport equation for the bulk species. The case of beam heating requires a mild upgrade: when fresh neutral beam source particles are continually injected, a steady state can only be reached if the particle loss equals the particle input. In case the density is assumed to remain the same and if the losses are represented by a simple constant particle loss time, this loss time is not a free parameter: it is prescribed by the local density and the beam source strength. But, there still is no need for an energy loss term.

https://doi.org/10.1017/S0022377821000234 Published online by Cambridge University Press

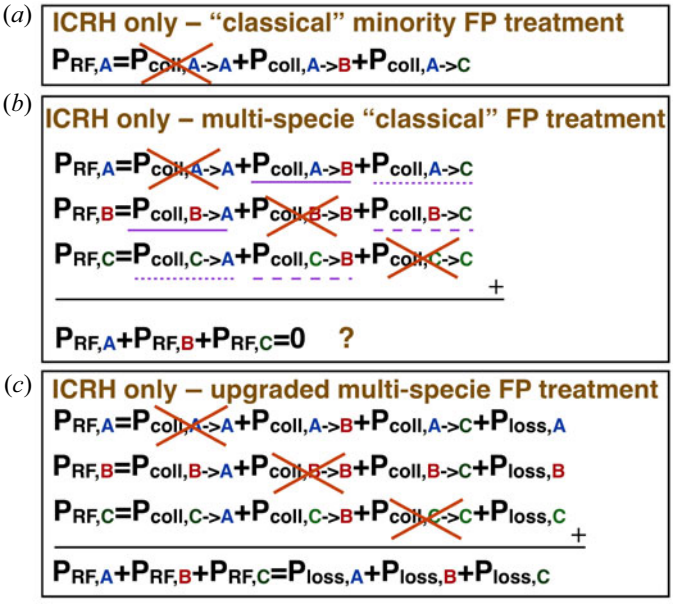


FIGURE 2. Philosophy classically used for minority RF heating (*a*), generalisation to all species (*b*) and inclusion of loss terms accounting for losses from local magnetic surfaces through radial diffusion (*c*).

When multiple populations are being heated and/or are interacting with each other, a set of coupled Fokker–Planck equations rather than a single Fokker–Planck equation needs to be solved. When including majority species in the set of populations described, self-collisions can no longer be neglected and the nonlinear collision operator for arbitrary distributions needs to be used. Since Coulomb collisions do not create nor annihilate particles or energy, the sums of all powers collisionally transferred from one specie to another is zero: the nonlinear collision operator $C(F_{o,A}, F_{o,B})$ describing collisional interaction between populations A and B satisfies the conservation relation $\langle C(F_{o,A}, F_{o,B}) + C(F_{o,B}, F_{o,A})\rangle = 0$ where $\langle \cdots \rangle$ denotes the energy integral over velocity space; $C(F_{o,A}, F_{o,B})$ is the collision term appearing in the Fokker–Planck equation solving for $F_{o,A}$ assuming $F_{o,B}$ is known, while $C(F_{o,B}, F_{o,A})$ is the collision term appearing in the Fokker–Planck equation solving for $F_{o,B}$. Adopting the generalised version of the logic sketched for a heated minority, this poses a fundamental problem (see figure 2*b*): whereas injected beam or wave power was flowing away to 'bulk' populations in the case of a single heated minority, hereby allowing a steady state – guaranteeing energy conservation – to be reached, there is now a net local energy influx but there is no net local energy loss. As a consequence it is impossible to reach a steady-state solution. So when describing the Coulomb collisional interaction between all species, an energy loss term needs to be introduced for a steady state to be reached, even when no beams are involved (see the bottom subplot of figure 2). The physical origin of this loss term is readily evident when looking at the 3-D Fokker–Planck equation: radial transport evacuates the local heat to neighbouring magnetic surfaces and the only global physical loss is power leaking out of the confined plasma across the last closed flux surface. That losses are an inherent part of magnetic confinement discharges is well known experimentally: to reach a steady state, the plasma needs to be replenished both by energy and particles.

https://doi.org/10.1017/S0022377821000234 Published online by Cambridge University Press

In the light of the realisation that the Fokker–Planck equation needs to include energy loss channels, we can now return to the isolated minority being heated and for which the introduction of a loss term was not deemed necessary. When a steady state is reached, the power collisionally transferred from the minority to the bulk ions and electrons has to be found back – up to a minus sign – in the power balance corresponding to the Fokker–Planck equations of these bulk species. For example, the bulk ions – which are assumed not to be directly heated by the waves when considering a single heated minority – now receive power from the minority. This power needs to be evacuated for a steady-state solution to exist. Note, however, that there is a shift in the reasoning: when solving the isolated Fokker–Planck equation for the minority, the steady state was achieved when the net effect of the RF waves was balanced by the net effect of the collisions. A higher density would for example give rise to more efficient evacuation of power and to lower tail energies. Also, at a prescribed density, a higher RF power yields higher energy tails. Solving the coupled Fokker–Planck equations for the minority and the bulk ions, the net effect of the collisions is cancelled out and the input RF power gain is ultimately compensated by a transport loss. So the local minority tail energy is partly determined by the amount of power locally deposited by the waves, as before, but also by the efficiency with which bulk energy is transported across magnetic surfaces. The proper choice of a suitable loss time τ_E for the Fokker–Planck equation is therefore crucial. Nor is the role of the collisions lost: the relative efficiency of the collisional transfer to the bulk ions and electrons determines which fraction of the power will be evacuated to each of the bulk populations. When multiple ion species are involved, the ultimate steady state depends on the relative strengths of the various collisional transfers as well as the loss channels and the strength of the power source. Adding losses to the Fokker–Planck equation – even when no beams are involved – is a deviation from what is traditionally done. It is a necessity when accounting for the Coulomb interactions of all species.

One possible way of defining a tau would be by connecting it with the local energy radial diffusion coefficient and local scale length, i.e. identifying the transport term $\partial/\partial\rho[\chi_{\rho\rho}\partial/\partial\rho\cdots]$ with the energy loss term $\cdots/\tau_E$ in the Fokker–Planck power balance equation. Transport is, however, not described by a single coefficient. At the very least some connection should be made with the conduction as well as the convection coefficient, both of which are typically finite. Moreover, since the transport and Fokker–Planck equations do not model the same populations (by construction, the transport equation strictly only models the Maxwellian subpopulations) a τ_E that is relevant for the thermal population is not necessarily suitable for the high-energy subpopulation. Rather than imposing a particular energy confinement time externally and as the focus of the present paper is on describing the impact of ICRH power on a discharge, the way the characteristic time τ_E is defined here is by ensuring that the loss term in the Fokker–Planck equation is consistent with the reigning transport. This is done by requiring that the initial (experimental) temperature is reproduced when solving the Fokker–Planck equation omitting the added RF power. Only in case no experimental data is available to permit deriving τ_E, it is imposed as an external parameter based on a suitable scaling law. It is implicitly assumed that τ_E does not vary too much when a finite amount of (supplementary) wave power is launched. Moreover, and not necessarily realistic, a single loss time has been adopted for the whole population whereas radial transport is expected to be different for thermal and high-energy subpopulations of a given population. The power locally lost is simply added to the self-collision's channel when composing the energy source terms fed into the transport solver. Since the losses represent radial transport and hence represent a loss of energy evacuated away from a magnetic surface to its neighbours, this step implicitly assumes the transport on neighbouring surfaces is similar so that the

https://doi.org/10.1017/S0022377821000234 Published online by Cambridge University Press

energy lost from a given surface is closely matched by the energy influx into it from the neighbouring ones.

7. Computation of the fusion rate

A key variable of interest for a heating scenario is the fusion power it allows to be produced. In this section it is described how the fusion rate for interacting arbitrary 1-D distributions $F_o(v)$ can be computed. The total fusion reactivity per unit volume is computed by evaluating

$$\langle \sigma(V)V \rangle = \int \mathrm{d}\boldsymbol{v}_1 \int \mathrm{d}\boldsymbol{v}_2 F_{0,1}(\boldsymbol{v}_1) F_{0,2}(\boldsymbol{v}_2) \sigma(V) V \tag{7.1}$$

in which $V = |\boldsymbol{v}_2 - \boldsymbol{v}_1|$ is the relative velocity. Approximate expressions exist for the reactivity. Adopting the parameterisation proposed by Bosch and Hale (Bosch & Hale 1992) allows us to write the reaction rate in the form

$$\sigma = \frac{S(E)}{E \exp(B_G/E^{1/2})} \tag{7.2}$$

in which

$$S(E) = \frac{A_1 + E(A_2 + E(A_3 + E(A_4 + EA_5)))}{1 + E(B_1 + E(B_2 + E(B_3 + EB_4)))}. \tag{7.3}$$

Here B_G is the relevant Gamov constant, E is expressed in keV and the resulting reactivity σ is given in mb (millibarn; $1\ barn = 10^{-28}\ \mathrm{m}^2$). For relevant fusion reactions, the values of the various constants can be found in Bosch & Hale (1992). The energy is defined via the reduced mass and the relative velocity $E = m_r V^2/2$ where $m_r = m_1 m_2/[m_1 + m_2]$. If one population is thermal while the other is fast, then (assuming species 2 is the slower population) $V \approx v_1$ and $E = [m_2/(m_1 + m_2)]E_1$. So while the maximal reactivity occurs at $E = 65$ keV, this maximum falls at $E_D = 108$ keV for the deuterons when the tritons are thermal, and at $E_T = 162$ keV for the tritons when the deuterons are thermal.

The cross-section only depends on the magnitude of the relative velocity and hence contains no information on the angular dependence. When assuming that the distribution functions themselves also only depend on the magnitude of the velocities of the two types of species, the computation of the integrated reaction rate can be simplified. Writing $\langle \sigma V \rangle$ explicitly in terms if spherical coordinates yields

$$\int_0^\infty \mathrm{d}v_1 v_1^2 \int_0^\pi \mathrm{d}\theta_1 \sin\theta_1 \int_0^{2\pi} \mathrm{d}\phi_1 f(\boldsymbol{v}_1) \int_0^\infty \mathrm{d}v_2 v_2^2 \int_0^\pi \mathrm{d}\theta_2 \sin\theta_2 \int_0^{2\pi} \mathrm{d}\phi_2 f(\boldsymbol{v}_2) \sigma(V) V. \tag{7.4}$$

Choosing the first axis of the second spherical coordinate system to be aligned with the first vector $\boldsymbol{v}_1$ (see figure 3) allows us to write $\boldsymbol{v}_2$ as

$$\boldsymbol{v}_2 = v_2[\cos\theta_2 \boldsymbol{e}_{//} + \sin\theta_2 \cos\phi_2 \boldsymbol{e}_{\perp,1} + \sin\theta_2 \sin\phi_2 \boldsymbol{e}_{\perp,2}] \tag{7.5}$$

where $\boldsymbol{e}_{//} = \boldsymbol{e}_{v_1} = \boldsymbol{v}_1/|\boldsymbol{v}_1| = \boldsymbol{v}_1/v_1$. We can rewrite

$$\begin{aligned} V = |\boldsymbol{v}_2 - \boldsymbol{v}_1| &= [(v_2\cos\theta_2 - v_1)^2 + (v_2 \sin\theta_2 \cos\phi_2)^2 + (v_2 \sin\theta_2 \sin\phi_2)^2]^{1/2} \\ &= [v_1^2 + v_2^2 - 2v_1 v_2 \cos\theta_2]^{1/2} \end{aligned} \tag{7.6}$$

from which it follows that $2V\,\mathrm{d}V = 2v_1 v_2 \sin\theta_2\,\mathrm{d}\theta_2$. When the distributions only depend on the magnitudes of the velocities then the only dependence on θ_1 and ϕ_1 is in

https://doi.org/10.1017/S0022377821000234 Published online by Cambridge University Press

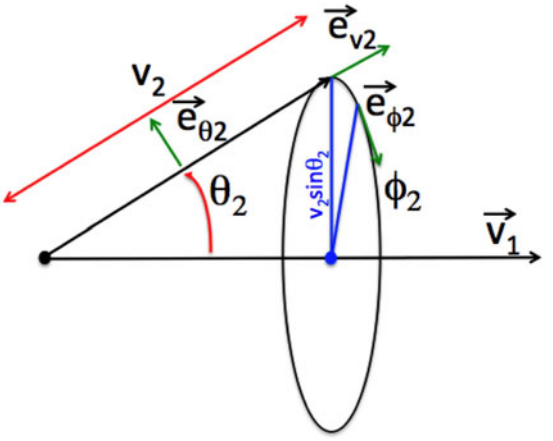


FIGURE 3. Unit vectors for spherical coordinates for which $\boldsymbol{e}_x$ is aligned with $\boldsymbol{v}_1$.

the Jacobian. The integral then can be reduced to

$$\langle \sigma(V)V \rangle = \int_0^\infty \mathrm{d}v_1 f_1(v_1) \int_0^\infty \mathrm{d}v_2 f_2(v_2) I(v_1, v_2) \tag{7.7}$$

in which

$$I(v_1, v_2) = 8\pi^2 v_1 v_2 \int_{|v_1 - v_2|}^{|v_1 + v_2|} \mathrm{d}V \sigma(V) V^2. \tag{7.8}$$

The latter integral can be tabulated once and for all on a grid on v-values, and a cubic interpolation allows us to approximate the values of the integral away from the grid points. Then using the trapezium rule to evaluate the integrals, the integral can be written as the vector–matrix–vector product

$$\langle \sigma(V)V \rangle = \boldsymbol{F}_{o,1} . \bar{\bar{A}} . \boldsymbol{F}_{o,2} \tag{7.9}$$

in which $F_{o,1,i} = F_{o,1}(v_i)$, $F_{o,2,j} = F_{o,2}(v_j)$ and

$$A_{i,j} = 8\pi^2 \left[v_i \Delta v_i\right] \left[v_j \Delta v_j\right] \left[I_o(|v_i + v_j|) - I_o(|v_i - v_j|)\right], \tag{7.10}$$

where

$$I_o(V) = \int_0^V \mathrm{d}V \sigma(V) V^2. \tag{7.11}$$

The total fusion yield can be computed fast by performing the above given integrals. As inputs, the distribution functions of the various interacting populations obtained by solving the coupled Fokker–Planck equations are used. Aside from the D–T, D–^{3}He and both the D–D cross-sections available in Bosch and Hale (Bosch & Hale 1992), the T–T cross-section has been included (Coster *et al.* 2010).

8. Example: 'baseline' (^{3}He) – D – T – D_{NBI} – T_{NBI} scenario

So far, this paper has been a rather technical report on fast tools available in EU-IM allowing the study of heating scenarios involving minorities as well as majorities and beams, all simultaneously – directly or indirectly – being heated by RF waves, energetic

https://doi.org/10.1017/S0022377821000234 Published online by Cambridge University Press

(neutral) particle injection and/or collisional interaction. In this section a single example is provided. The accent is on illustrating the type of output generated rather than making a deep physics study, the reason being that the accent of ETS and EU-IM publications is typically on the latter while assuming knowledge about the modules behind has been advertised elsewhere. The interested reader desiring to have more insight in the EU-IM framework on the one hand or on actual physics application on the other is referred to papers listed at the outset.

Now, JET is preparing for a second D–T experimental campaign (DTE2), see for example Garzotti *et al.* (2019); Joffrin *et al.* (2019). The first (DTE1) campaign, executed in the1990s, showed that fusion could be realised abundantly in JET (see for example Jacquinot *et al.* 1999; Keilhacker *et al.* 1999; Start *et al.* 1999). One major difference between the JET machine back then compared with now, is the presence of the ITER-like wall (Philipps *et al.* 2010; Joffrin *et al.* 2014). A key motivation for moving away from a carbon wall was for better control of the in-vessel tritium (T) inventory, crucial in ITER to meet regulatory requirements, plasma-facing components having a very high hydrogen fuel retention. One of the first key results from JET–ILW was the confirmation of low retention of hydrogen fuel compared with JET-C, see for example Brezinsek *et al.* (2013). The beryllium wall and tungsten divertor have significantly modified the boundary conditions of experiments. One issue to be tackled is the potential of accumulation of high Z material in the core. Core concentrations of tungsten larger than a few 10^{-4} cause the core temperature to collapse when not enough auxiliary heating power reaches the centre to compensate the high radiation. Significant radiation is also observed close to the low field side edge of the plasma, attributed to tungsten accumulation resulting from interaction with the W divertor or W-covered surfaces (e.g. the NBI dump plates to protect the machine against shine-through) in the machine. The temperature collapse in the core can result in a global thermal quench provoking a disruption. Ion cyclotron resonance heating has shown to ensure high Z particles are expulsed from the core (Goniche *et al.* 2014; Lerche *et al.* 2015; Van Eester *et al.* 2016*b*) although a demonstration in D–T relevant circumstances still needs to be done. Apart from providing input for ITER, one of the goals of the second D–T campaign is to demonstrate that the results obtained in the carbon wall machine can still be achieved in presence of a metal wall. Progress in understanding has, however, led to the hope that the then set standards can be bypassed: a key target of DTE2 is the demonstration of sustained DT fusion power of 10 to 15 MW for 5 s (Litaudon *et al.* 2017). A 'key performance indicator' (known as KPI) used to monitor the progress of plasma preparation in deuterium was the sustained D–D neutron rate, with a target of 5×10^{16} n s^{-1} (equivalent D–D neutron performance of a plasma capable of 15 MW DT power, according to 0–D calculations with assumption on $H_{98(y,2)}$).

Neutral beam injection is JET's dominant heating scheme: in the recent campaigns it was shown that 32 MW of beam power can be launched into the JET plasma making use of beam energies of approximately 120 keV. Switching off the beam to terminate the shot has shown to hold a risk: the particle and the energy confinement time not being the same, the core temperature typically starts dropping faster than the core density. To counteract – similar to what was discussed above for the main heating phase – the collapse of the temperature profile, a heating well localised in the core is needed after the main heating has been switched off. While beam deposition profiles are commonly very wide (the beam ionisation starts taking place as soon as the neutral beam penetrates a plasma of sufficient density), ICRH can deposit power in a much more localised way. For that reason, ICRH has become of the tool of reference to chase high Z impurities from the core and to 'land' JET

https://doi.org/10.1017/S0022377821000234 Published online by Cambridge University Press

discharges (Goniche *et al.* 2014; Lerche *et al.* 2017; Litaudon *et al.* 2017). Understanding the interplay between NBI and ICRH is crucial for optimising high performance JET shots.

The preparations of a D–T campaign have highlighted two main candidates for reaching the goal set: the 'baseline' scheme (see for example Kim *et al.* 2018) operates at high magnetic field B_o and current I_p while maintaining a high plasma density N_e. As high B_o and I_p require a high auxiliary heating power, this scheme tends to operate at a modest normalised β. It holds the promise for a long stationary state but suffers from a somewhat high disruption rate, and tends to have MHD activity (fishbones and NTMs, the latter more often than not triggered by violent sawtooth crashes) that degrade its performance. The 'hybrid' scheme (see for example Joffrin *et al.* 2005) relies on current profile tailoring, and typically operates at higher normalised β. Because of its higher safety factor this scheme does not have sawtooth crashes and suffers less from disruptions.

The RF heating scheme currently mostly used during the ongoing preparations has been the RF 'work horse' since the machine's inauguration in 1983: core fundamental cyclotron heating of an H minority in a D plasma. The neutral beam injectors are typically injecting deuterium, and hence the latter as well as the main ion species absorb power in the plasma centre close to their second cyclotron harmonic layer. In the actual D–T campaign, half of the majority D will be substituted for T. It was shown in DTE1 that adding a small amount of ^{3}He to the plasma mix and heating it with ICRH boosts the neutron rate significantly. A ^{3}He minority can be equally be heated at its fundamental cyclotron layer in JET, this forming with T a pair such as (H)–D as the second harmonic T cyclotron layer coincides with the fundamental cyclotron layer of ^{3}He. Both the baseline and the hybrid scenarios operate in H-mode.

In what follows the various simulations will be loosely based on the JET experimental baseline shot 92436 but rather than the plasma composition of that shot (H minority in a D majority plasma in which a D beam is fired) we will consider the case of a ^{3}He minority in a balanced D–T majority in which balanced D and T beams are injected. The minority concentration is taken as in the reference experiment ($\approx$1.6 % in the core) while the beam concentration for each of the beam boxes is of the order of 2–3 %. The adopted density and temperature profiles for the bulk species are depicted in figure 4. The central electron density is $N_{e,0} \approx 7\text{–}8 \times 10^{19}$ m^{-3} while the density at the pedestal is $N_{e,0} \approx 4.5 \times 10^{19}$ m^{-3}, the central electron temperature is $T_{e,0} \approx 8$ keV. Since there is no experimental ion temperature data in the actual core (the closest T_i data point is approximately 20 cm from the centre), the ion temperature profiles adopted for the present example (with core ion temperatures reaching $T_{i,0} \approx 11$ keV) have been computed inside ETS when solving for the ion heat equation using power density input profiles provided by the tools discussed in the present paper. When modelling the original JET baseline scenario, the computed ion temperature matches the experimentally found values in regions where experimental data is available (Huynh *et al.* 2020). Hence – although the plasma composition is vastly different – there is some confidence that the obtained profiles are reasonable, one reason being that the wave polarisation dynamics associated with the (^{3}He)–T pair (sharing the same cyclotron damping region, the former for minority fundamental and the latter for majority second harmonic heating) is similar to that of (H)–D in the reference shot. More details on this computation as well as a deeper study of the DT scenarios choosing either H or ^{3}He as minorities can be found in Huynh's paper. The toroidal magnetic field strength is $B_o = 3.28T$ (adapted to ^{3}He core heating and hence differing from the actual B_o in shot 92436) while the plasma current is $I_p = 3MA$. The effective beam power (after subtracting for example charge exchange and shine-through losses) of the reference shot was approximately $P_{\mathrm{NBI}} = 26$ MW while the RF power was $P_{\mathrm{RF}} \approx 5$ MW. In the present example, the D beam is substituted by a D and a T beam.

https://doi.org/10.1017/S0022377821000234 Published online by Cambridge University Press

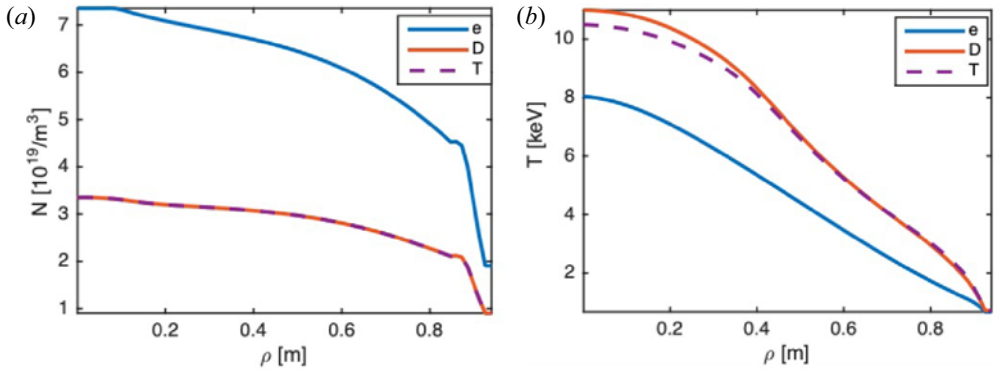


FIGURE 4. Density and temperature profiles of the bulk species.

The energy of each D injector is taken to be $125keV$ and that of each T injector is 118 keV, the latter lower than the maximum possible voltage in view of engineering restrictions for safe operation. Each beam has a full-energy, a half-energy and a third-energy component. For launching the RF waves, dipole phasing was exploited and the driver frequency was chosen to be 33 MHz (aiming to heat the ^{3}He minority and the T majority) to ensure core ion heating for the adopted magnetic field.

To compute the beam source profiles, ASCOT (Hirvijoki *et al.* 2014) was used, while CYRANO (Lamalle 1994) was exploited for describing the wave propagation and collisionless damping on various populations. Next, StixReDist (Van Eester & Lerche 2011) and FoPla (described earlier) were used for computing the respective distributions of the various interacting populations, the former for test particle populations that do not have a beam source, the latter for the ones that do.

Figure 5 depicts the ICRH and NBI power deposition profiles. Panels (*a*, *b*) show the RF power flowing to various of the species for a total incoming RF power of 5 MW. The power density peaks slightly away from the core. The ^{3}He minority is the most efficient absorber (47 %). Sharing its second harmonic layer with the fundamental cyclotron layer of the minority is the majority T, it absorbs 24 % of the incoming RF power. Also the highest energy T beam absorbs some of the power (5 %). The bulk D has its fundamental cyclotron layer on the high field side yielding the D absorption maximum at $\rho \approx 0.65$ m. These species absorb 10 % of the incoming waves power. The other ions absorb very little wave power. The electrons, finally, have a wide deposition profile but have their highest power density near the plasma core; 11 % of the power flows from the waves to the electrons.

Figure 5(*c*, *d*) shows the deposition profiles of the various beam populations. There are six populations in total, three of which correspond to the D beam and three to the T beam energy components. The beams are composed of a dominant beam fraction launched with an energy of 125 keV (D) or 118 keV (T), a fraction that is launched at half that energy and a small fraction, finally, that is launched at 1/3 of the energy. The highest energy beams (both D and T) penetrate deepest into the plasma and have a deposition profile that peaks close to the centre. In contrast, the lowest energy beams ionise close to the plasma edge and hence have a density that peaks there. The deposition profile of the half-energy beams is roughly flat throughout the cross-section. Most of the beam energy is carried by the high-energy beams; the full energy component also has the highest density. Especially the third-energy beam is a mere correction to the deposition of the full-energy beam component.

https://doi.org/10.1017/S0022377821000234 Published online by Cambridge University Press

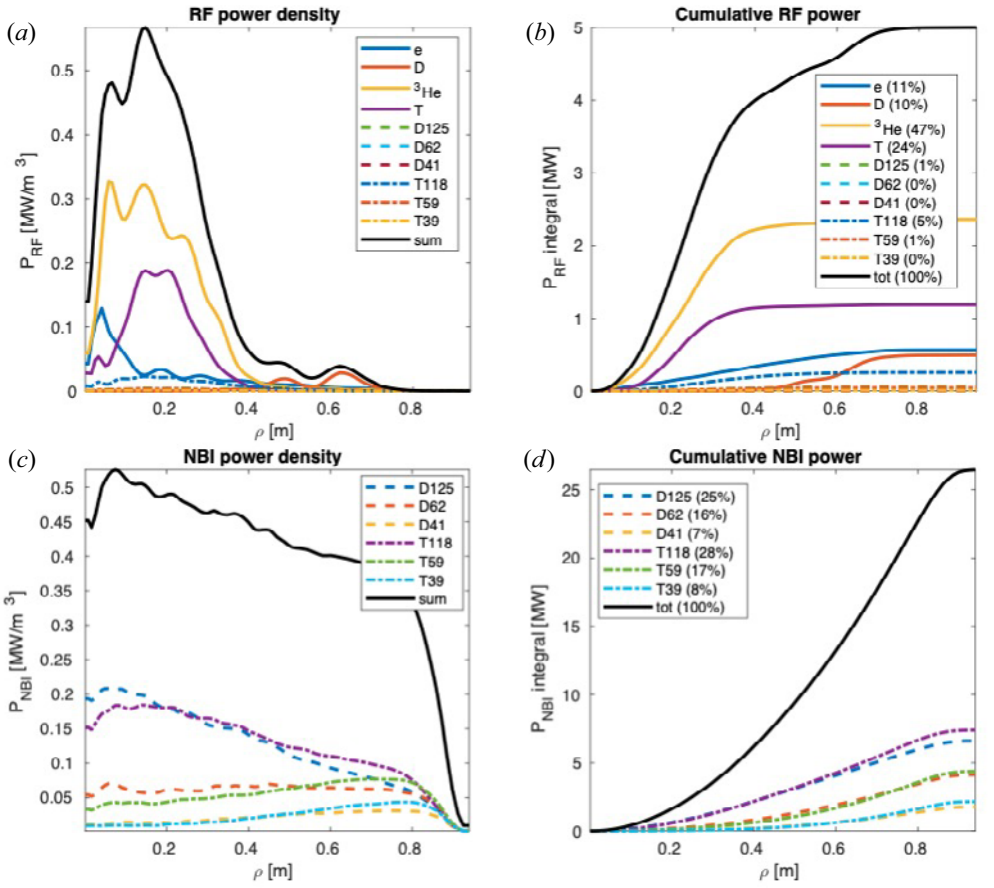


FIGURE 5. The ICRH and NBI local and integrated power deposition profiles for a total integrated beam power of 26 MW and RF power of 5 MW.

Although the RF power level is much lower than that of the beams, the RF power density is of the same order of magnitude as that of the beams in the core. This is a consequence of the fact that RF heating is well localised and that core wave heating was envisaged. Because the beam deposition profile is determined by ionisation of the incoming neutral beam, and since the plasma density is high (and fairly flat), the beams start depositing power as soon as they penetrate the plasma, yielding a very wide deposition profile. Since power lost closer to the edge is smeared out over a large volume, the corresponding power density is low in spite of the beam power being a factor of six higher than that of the RF waves. As a result of the relative magnitude of the contributed power densities it is fair to say that the width of the temperature profile is mainly set up by the beams while core localised RF power allows to have a significant impact in the highest density, highest temperature region of the plasma.

Figure 6 shows how the beam power is collisionally redistributed in 'absence' of RF power. Since the power densities remaining in the beam populations is very modest, these contributions have not been retained in the plot. Because the critical energy (at which the population that is slowing down passes on half of its energy to the electrons and half to ions; $E_{\mathrm{crit},j} = 14.8kT_e(eV)A_j(\sum_i X_i Z_i^2/A_i)^{2/3}$ where X_i is the concentration and the index

https://doi.org/10.1017/S0022377821000234 Published online by Cambridge University Press

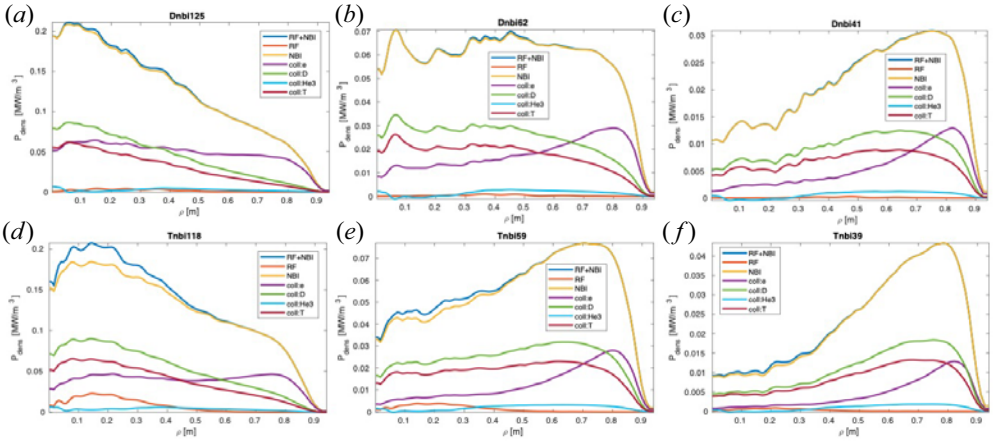


FIGURE 6. Coulomb collisional power distribution of the various beam species considered in absence of ICRH power.

i loops on the various ion populations while the index *j* refers to the test species) scales with the electron temperature, electrons tend to receive more of the beam power closer to the plasma edge. Higher energy beams tend to pass on a bigger fraction of their power to the electrons, their energy exceeding the critical energy more. The combination of the two effects results in high-energy beams heating both ions and electrons in the core while the lower energy beams favour ion heating. When including all beam energies, ion heating is dominant in the core. Near the edge, the high-energy beams mainly crank up the electron temperature. For the lower energy beams, ions and electrons play a similar role towards the outer layers of the plasma. Here, electron heating is the dominant effect. Note that the deuterium is systematically favoured over the tritons for heating via Coulomb collisional power transfer. The reason for this behaviour is related to the relative mass: because T is more massive, its thermal velocity for the same temperature is smaller. Hence, fast populations slowing down will first collisionally interact with D ions and only afterwards with T ions. This is true independent of which is the fast subpopulation.

The fate of energy carried to the core of the plasma by waves is critically dependent on the RF power density. Lower power densities prevent high-energy tails being formed and hence favour RF power flowing to the ions. Higher levels of wave power launched allow the transfer of more power to the electrons. This is clearly illustrated in figure 7, depicting the total RF+NBI Coulomb collisional power redistribution for four different RF power levels: 0.1, 3, 5 and 7 MW at constant $P_{\mathrm{NBI}} = 26$ MW beam power. Again, the modest power flowing to the beam populations has been omitted in the plot. At low power each of the core bulk ions receives double the power flowing to the electrons, in agreement with the pure NBI heating case shown in figure 6. When the RF power level is $3MW$, the core power density is significantly higher than that in absence of ICRH. Also, the power density collisionally passed on to the bulk ions shows a distinct peak. When 5 MW of RF power is coupled to the plasma, the electron power deposition also peaks. Compared with what was the case in absence of RF power, the electrons now receive almost three times more power in the core. This effect becomes gradually more pronounced if even higher RF power levels can be achieved. The extra power is now preferentially flowing to the electrons. The combined heating of electrons and ions in the core allows the boosting of the core temperatures, the RF + NBI power density exceeding the NBI-only power density

https://doi.org/10.1017/S0022377821000234 Published online by Cambridge University Press

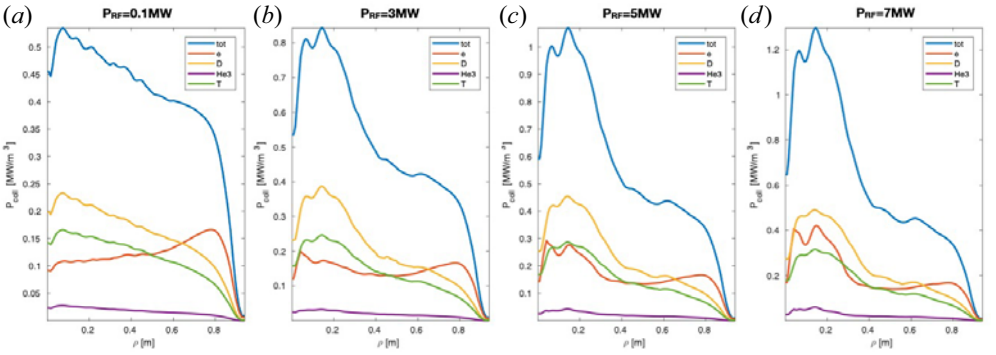


FIGURE 7. Collisional power redistribution for four different ICRH powers launched: 0.1, 3, 5 and 7 MW. The beam power is the same for all cases: 26 MW.

by a factor two or more in spite of the most amount of RF power compared with that of the beams. As noticed before, the deuterons are receiving more power than the tritons. The increased electron heating has an indirect but very important effect: increasing the electron temperature increases the critical energy and allows more of the beam power to flow to the ions, allowing a further boost of the ion temperature.

Figure 8 zooms in on the redistribution of the two ions receiving most of the incoming wave power: the ^{3}He minority and the T majority. There is a distinct difference between the two behaviours. While the minority passes on similar amounts of power to the electrons and each of the bulk ion species (so that the bulk ion heating dominates the electron heating), the tritons heat the ions much more than they do the electrons. Since T is heated at its second harmonic, this comes as a surprise at first: second harmonic heating creates highly energetic tails and leaves the thermal region untouched. The reason is twofold. (i) Since various populations absorb a part of the power, the power densities are relatively modest and the tails are not particularly energetic, allowing to contribute to ion rather than electron heating. (ii) As mentioned before, the beam is the dominant heater of the plasma. Slowing down beam particles feed energy to the thermal population and increase its temperature. Because the results shown are not the result of solving a standalone Fokker–Planck equation for the beam but of solving the coupled set of equations while accounting fully for collisional interaction of the various species (including self-collisions of the majority population), the ion thermal temperature is being pushed up to higher values. Note that opposite to 'pure' slowing down which was more of benefit to D rather than to T ions, it is now the tritons that receive most of the redistributed power, partly through the loss term (radial diffusion was assumed to vary little between neighbouring magnetic surfaces, allowing us to identify the radial diffusion loss to neighbouring surfaces with the radial diffusion gain of power from these neighbouring surfaces) and since the tritons absorb wave power themselves. This underlines that single specie reasoning and multi-specie reasoning are different.

What sets the ICRH modelling presented here in the EU-IM framework apart from usual ICRH modelling is best illustrated by figure 9: whereas heating scenarios commonly involve various populations exchanging energy via Coulomb collisions, this aspect is commonly unaccounted for. Presenting a method allowing the study of the simultaneous heating of minorities, majorities and beams while accounting for their collisional interaction is a key point of attention in the present paper. For the baseline scenario at hand, nine ion populations interact, none of which is untouched by either the beam or

https://doi.org/10.1017/S0022377821000234 Published online by Cambridge University Press

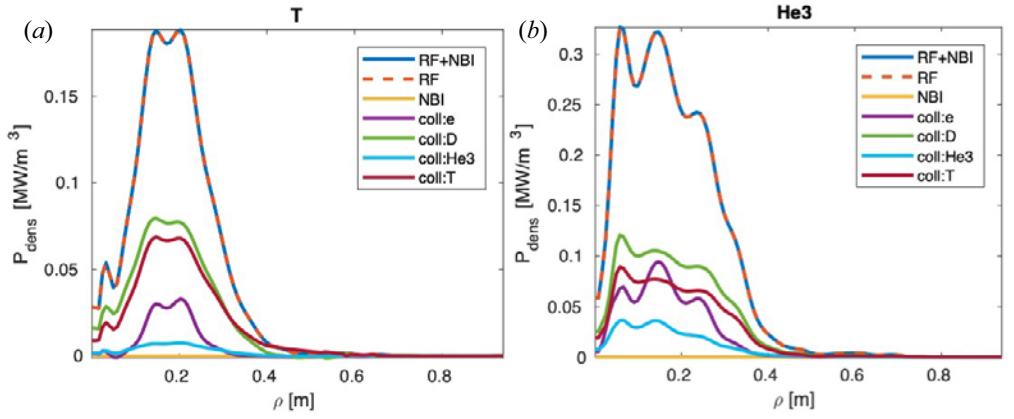


FIGURE 8. Coulomb collisional power distribution of the core RF heated non-beam species T majority and ^{3}He minority for a total integrated RF power of 5 MW.

the RF heating or both. The T ions are heated through ICRH and receive power from ^{3}He and, to a lesser extent, beam D and T ions slowing down. In the core, D ions are purely heated by collisions. The D heating on the far high-field side occurs in a region where drawing high-energy tails is inefficient. In the present paper the electron distribution function has not been evolved. There are two reasons for this: (i) expressed in terms of the velocity (the strength of Coulomb collisions is determined by the relative velocity) the electron distribution is very wide. Certainly in high density plasmas, ICRH is unable to deviate the electron distribution much from its Maxwellian character and it is sufficient to feed the power flowing to the electrons to the transport equation which describes how the macroscopic temperature changes under the influence of radial diffusion, local sources and losses. (ii) Because there is little overlap between the electron and the ion distributions, it takes many more iterations to reach a steady state when evolving the electron distribution function together with that of the ions (this was discussed and illustrated in Van Eester & Lerche (2011)). Moreover, electrons easily reach speeds for which relativistic effects need to be accounted for in high temperature plasmas. The numerical grid required to solve the relevant Fokker–Planck equation for the electrons is very different from that required for the ions. One subtlety to keep in mind when omitting the changes in the electron distribution is that one cannot blindly use the electron contribution to the expressions for the collision operator on a grid suitable for the ion distributions: because most of the electron distribution is cut off, an extra contribution

$$D_{vv}^{a/e,\mathrm{extra}} = \frac{4\pi\Gamma^{a/e}}{3N_e}\int_{v_{\max}}^{\infty} \mathrm{d}ppF_{o,e}(p) = \frac{4\pi\Gamma^{a/e}}{3N_e} v_{\mathrm{th},2}^2 F_{o,e}(v_{\max}) \tag{8.1}$$

has to be added to the diffusion coefficient of the ion collision operator when computing the operator numerically; $v_{\max}$ is the highest velocity grid point considered for computing the ion distributions. This term dominates the contribution added at lower velocities and hence omitting it represents an underestimation of the diffusion ions undergo. Whereas the convection/friction term in the collision operator forces a slowing down, diffusion allows small fractions of particles to gain energy via Coulomb interaction.

Having obtained the distribution functions of all ion species on all magnetic surfaces $F_{o,i}(v, \rho)$, the local fusion power densities can be computed using the expressions for the total fusion rates accounting for the Bosch & Hale cross-sections for the various nuclear

https://doi.org/10.1017/S0022377821000234 Published online by Cambridge University Press

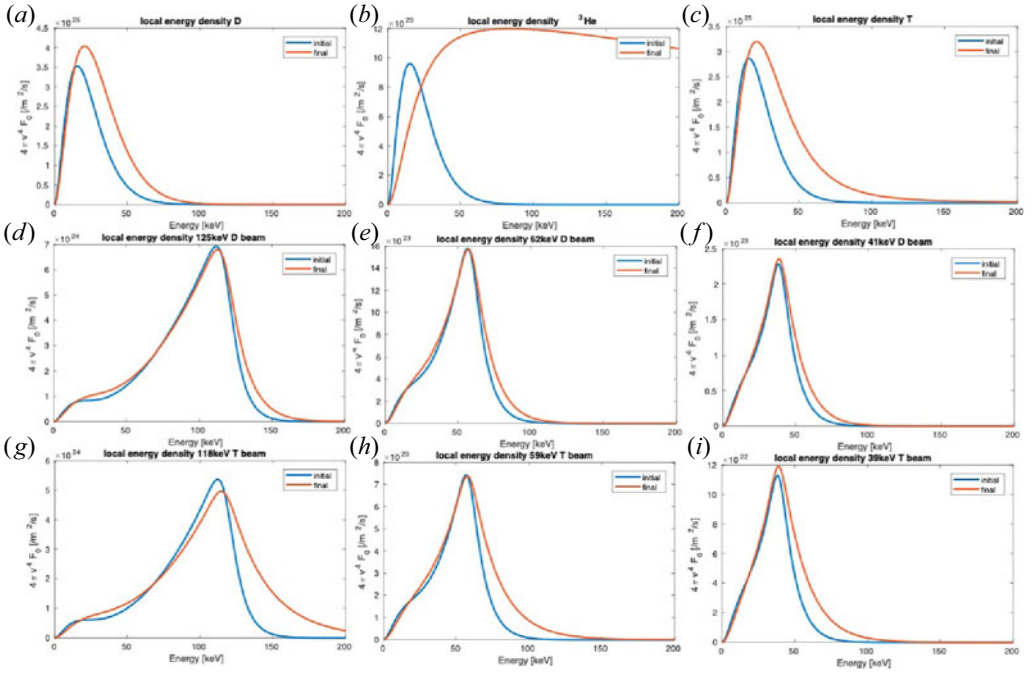


FIGURE 9. Distribution functions of all ion species at $\rho = 146$ mm.

fusion reactions adopting the method described in § 7. Figure 10 depicts an example in which D–D, D–T as well as T–T fusion reactions have been accounted for, considering the actual distribution functions of the interacting species on each magnetic surface. For a given distribution, no distinction is made between the thermal part and the suprathermal part. The contribution from the bulk ions is dominant in baseline discharges with moderate β. The contributions due to the interaction between the bulk species and the beams are adding a substantial contribution as well. Note that the contribution due to the D beam interacting with the T bulk dominates that of the T beam interacting with the D bulk, suggesting that using pure D beams is more beneficial than a mix of D and T beams even when D is not directly heated. One of the reasons is that it is likely that $N = 2$ heating forms a high-energy RF heated beam tail which is counterproductive for the fusion yield since it is at too high energy to add a contribution. Recall for example that the optimal equivalent Maxwellian temperature for T to contribute to the D–T reaction is 162 keV while it is 108 keV for D ions and 65 keV when suprathermal populations of both exist. In contrast, the D beam is not heated directly by the RF waves but contains a thermalised slowed down contribution with a temperature higher than that of the corresponding T. Also, because of its heavier mass, the thermalised subpopulation of the bulk T ions is shifted to lower velocities than that of the bulk D so that any accelerated population slowing down on the bulk ions is more likely to interact with the D than with the T particles. Aside from the D_{bulk}–T_{bulk}, D_{bulk}–T_{NBI} and T_{bulk}–D_{NBI}, all other contributions to the neutron rate are negligibly small.

The net effect of the ICRH–NBI synergy can be seen in table 1 where the fusion yield for four different ICRH powers has been summarised. The first point to notice is that the dominant fusion yield indirectly (i.e. via Coulomb collisions) comes from the beam: when the wave power is negligible compared with the beam power, the fusion yield is

https://doi.org/10.1017/S0022377821000234 Published online by Cambridge University Press

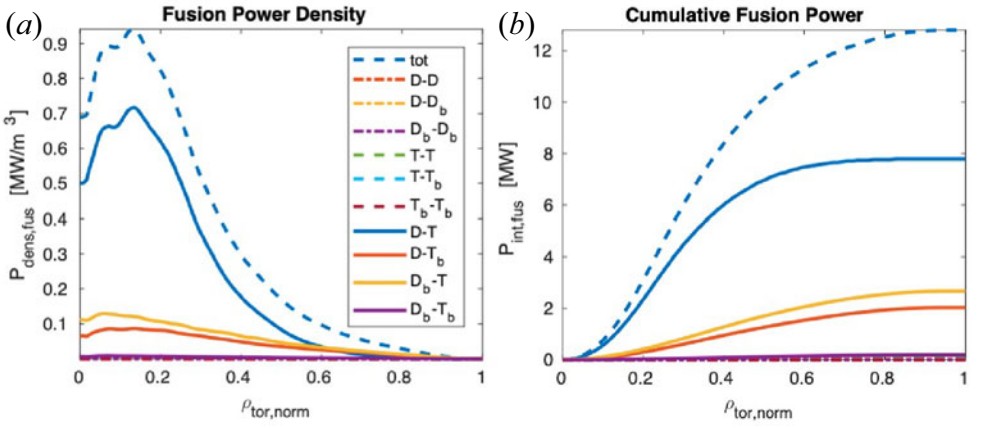


FIGURE 10. Fusion power density profile for the case when 5 MW of RF power and 26 MW of beam power is launched into the JET plasma.

already ≈11 MW. Adding RF power, this number is growing for growing applied RF power through the individual increases from the various contributions (bulk D–bulk D, bulk D–beam D, . . .) but the dominant contribution comes from the fusion reactions between the bulk species. The latter fusion rate is modified for two reasons: (i) the temperature of the thermal subpopulation has increased and (ii) suprathermal ion tails have been formed. For a fusion reaction with a distinct maximum near the temperature naturally reached by freshly injected beam particles, the second harmonic RF heating of the bulk as well as beam species creates tails that have energies too high to be of benefit for producing fusion reactions. The main mechanism through which the fusion reactions are triggered is the medium high and high-energy particles slowing down and boosting the temperatures of the thermal subpopulations. Through the use of ^{3}He, the bulk ion temperature can be increased (^{3}He being more massive than H, it tends to slow down more on ions than H does). Also electron heating is beneficial for boosting the ion temperature: increasing the critical energy allows more of the beam power to be transferred to the ions.

It is important to point out that the present computations only zoom in on ICRH and NBI aspects. In practice, MHD activity, changes in transport and radiation play a key role. The goal of the EU-IM platform is exactly to incorporate all such effects as best as possible when studying scenarios. As the present paper only focussed on the description of the auxiliary heating and ended at providing source terms for the transport equations (power deposition profiles after Coulomb collisional redistribution of incoming wave and beam power) rather than actually integrating them, the numbers given are inherently connected to the starting assumptions made and hence are only partial. Aside from dynamics fully omitted here, also the parameters related to the ICRH and beam sources themselves are of importance. In the present paper a single concentration and a single minority specie was considered. Exploiting ETS and assuming $P_{\mathrm{RF}} = 5$ MW, Huynh finds the fusion power drops from 13–14 MW when the minority concentrations are very low ($N_{\mathrm{minority}}/N_e < 1\,\%$) to 8–10 MW when they are increased beyond the values usually used in the experiments ($N_{\mathrm{minority}}/N_e \approx 5\,\%$), and this – although details differ – both when using H or ^{3}He (but adopting the appropriate RF frequency to ensure core heating) (Huynh *et al.* 2020), suggesting the formation of high-energy tails is beneficial but mainly pointing to the fact that fuel dilution is counterproductive. Finally, since the bulk ion temperature is the most important parameter in determining the fusion yield, any means of modifying the bulk

https://doi.org/10.1017/S0022377821000234 Published online by Cambridge University Press

P_{RF} [MW]:	0.1	3	5	7	unit
D–D	0.0583	0.0670	0.0737	0.0787	[10^{17} n s^{-1}]
D-D_{NBI}	0.0437	0.0454	0.0466	0.0475	[10^{17} n s^{-1}]
D_{NBI}-D_{NBI}	0.00243	0.00249	0.00254	0.00257	[10^{17} n s^{-1}]
T–T	0.147	0.171	0.193	0.214	[10^{17} n s^{-1}]
T-T_{NBI}	0.0904	0.0950	0.0985	0.1020	[10^{17} n s^{-1}]
T_{NBI}-T_{NBI}	0.00441	0.00457	0.00469	0.00481	[10^{17} n s^{-1}]
D–T	20.8	24.8	27.7	29.9	[10^{17} n s^{-1}]
D-T_{NBI}	6.71	7.01	7.23	7.41	[10^{17} n s^{-1}]
D_{NBI}-T	9.17	9.36	9.49	9.60	[10^{17} n s^{-1}]
D_{NBI}-T_{NBI}	0.655	0.666	0.674	0.681	[10^{17} n s^{-1}]
Total *n* rate	37.7	42.2	45.5	48.0	[10^{17} n s^{-1}]
P_{fusion}	10.61	12.89	12.82	13.53	[MW]

TABLE 1. Partial (per source pair) and total (summed over all pairs) neutron rate in 10^{17} n s^{-1} and corresponding total generated fusion power in MW for four different RF power levels: 0.1, 3, 5 and 7 MW.

temperature considered will impact on the fusion yield obtained. Remembering that core ion temperatures are not available experimentally in JET, correctly predicting the bulk ion temperature is therefore crucial. The inital temperatures considered here are provided by ETS runs. Repeating the above exercise starting from a plasma that starts from a core electron temperature of 7 keV and an ion temperature of 8.5 keV – the temperatures reached only exploiting the beams – reduces the fusion achieved power from the values in the above table to 7.69, 8.58, 9.20 and 9.70 MW for an added RF power of 0.1, 3, 5 and 7 MW, respectively. The D–T contribution from the thermal bulk populations is roughly half of the fusion yield but is gradually increasing with the RF power level. For the adopted power levels it is 44 %, 48 %, 51 % and 53 %, respectively. This very mild increase – even the maximum RF power considered is modest compared with that of the beams – possibly reflects the fact that the applied wave power helps raise the ion temperature, partly since more power is directly absorbed by the ^{3}He minority, which dumps a fraction of its power onto the bulk ions. More generally, wave power can collisionally end up in the bulk ion channel, the total RF power density being distributed over various species and remaining fairly modest, and a fraction of the beam energy being channelled to the ions on their slowing down (see figures 7 and 8). Studying fusion enhancement brought about by ICRH in a DT plasma but using a much more sophisticated Fokker–Planck model than the one adopted here but only considering one (RF) heated non-Maxwellian population at the time while prescribing the density and temperature, Harvey equally found a very mild increase of the enhancement when reaching higher power densities for JET-relevant densities and temperatures when accounting for the observed mild temperature increase (see figure 5 in Harvey *et al.* (1986)). At very high power densities (not reached at JET by any of the heated species) he observes a rollover caused by the optimal operation point being passed.

9. Conclusions

The present paper is devoted to the discussion of recent upgrades of one of the Fokker–Planck modules available in the EU-IM framework used in the ETS which allows the solving of sets of coupled Fokker–Planck equations – modelling minorities,

https://doi.org/10.1017/S0022377821000234 Published online by Cambridge University Press

majorities and beam populations simultaneously heated and all interacting collisionally with each other – rapidly while making reasonable simplifications. Simulating entire discharges necessarily requires introducing simplifications. It goes without saying that detailed aspects are beyond the scope of the modules discussed and adopted here. For detailed insight into specific aspects, the use of more complete simulation models requiring significantly more CPU time is required. The two types of codes are complementary. The exploited forms of the Fokker–Planck equation are provided; some details on the adopted methods to solve the equations are provided in two appendices. Through a proper choice of input flags, the various versions of the Fokker–Planck equations as well as solvers can readily be exploited on the EU-IM platform. A brief section is also devoted to provide the procedure for evaluating the fusion rate for arbitrary distributions used to estimate the fusion power using the solutions of the set of Fokker–Planck equations.

The paper closes by providing a practical example of the use of the described modules: a simulation of the D–T JET 'baseline' scenario involving nine ion (minority ^{3}He, majorities D and T and full-, half- and third-energy D and T beams) populations that are simultaneously heated by neutral beam injection and RF waves, necessitating accounting for Coulomb collisional interaction of multiple non-Maxwellian distributions. It is shown that the fusion yield is mainly due to the plasma heating by the beams and that the slowing down process cranking up the temperature of the thermal subpopulation of the various fuel ion populations is crucial. It is also demonstrated that a few MW of RF power can locally significantly modify the deposition profiles allowing us to provide well-localised heat sources allowing us to further boost the core temperature profile, partly through the wave heating itself but equally – when accounting for electron temperature changes solving the transport equations – due to the fact that energetic tails slow down on electrons and hereby increase the critical velocity so that more beam power ultimately ends up in the ion channel. This effect allows a further enhancement of the ion temperature, of benefit for the fusion yield. Finally, the direct acceleration of the majority T ions by ICRH and their collisional redistribution to the D ions has shown to also play a significant role, allowing for a further enhancement of the total fusion power produced in JET D–T discharges. The present paper did not involve the full *ETS* framework and focussed on documenting adopted procedures rather than providing an in-depth physics study. Exploiting ETS both for interpretative studies of the 92436 D–D JET baseline shot adopted here, and then proceeding to interpretative runs both for D– and D–T, Huynh made a physics study of the ICRH–NBI synergy and its potential for DTE2, both for scenarios relying on an H as on a ^{3}He minority (Huynh *et al.* 2020).

Acknowledgements

This work has been carried out within the framework of the EUROfusion Consortium and has received funding from the Euratom research and training programme 2014-2018 and 2019-2020 under grant agreement no. 633053. The views and opinions expressed herein do not necessarily reflect those of the European Commission.

Editor Christos Tsironis thanks the referees for their advice in evaluating this article.

Declaration of interests

The authors report no conflict of interest.

Appendix A. Finite element solving

Having in mind the form of density and energy conservation checks, the Fokker–Planck equation to be solved is multiplied by a test function G as well as the Jacobian factor v^2

https://doi.org/10.1017/S0022377821000234 Published online by Cambridge University Press

and integrated over a chosen volume. After performing a partial integration one gets

$$-\int \mathrm{d}v \frac{\partial G}{\partial v}\left[A(v)\frac{\partial F_o(v)}{\partial v}+B(v)F_o(v)\right]+\int \mathrm{d}vGv^2S+\int \mathrm{d}vGv^2CF_o=0 \qquad \text{(A1)}$$

where $C=-1/\tau_p$ and in which it has been anticipated that suitably smooth 'hat' functions will be used such that two neighbouring finite elements are treated together such that the inner flux is continuous – and thus does not show up – and the flux at the outer ends is zero since the projection function is. A simplified procedure to isolate the effect of fast particles consists of using a Taylor or an asymptotic expansion of the error function and its derivative in the expressions for the Coulomb relaxation (Gaffey 1976). The statement that the surface terms give no contribution is not true at the origin for that case: the collision operator has a sink at $v=0$, the advantage being that the slowing down time terms are no longer needed (as is for example the case for the slowing down distribution which can be obtained when the later discussed simplification is made). For that case – as well as for the case where base functions are used that are not sufficiently continuous – the surface terms need to be retained in the equation.

It is preferred here to avoid discontinuities, though. To ensure the proper continuity, third-order polynomial local base functions are used in each element and F_o is written as a linear combination of these four independent functions. Introducing a local coordinate $\xi=(v-v_i)/(v_{i+1}-v)=(v-v_i)/\Delta_v$, the four base functions $G(\xi)$ exploited either have a unity value or derivative at either of the edges, the remaining ones remaining zero (e.g. $G_1(0)=1$, $G_1(1)=0$, $\mathrm{d}G_1/\mathrm{d}\xi(0)=0$, $\mathrm{d}G_1/\mathrm{d}\xi(1)=0$). Solving these four systems of four equations yields the coefficients of the polynomials. One gets $G_1=1-3\xi^2+2\xi^3$, $G_2=3\xi^2-2\xi^3$, $G_3=\xi-2\xi^2+\xi^3$ and $G_4=-\xi^2+\xi^3$. In the interval $[v_i, v_{i+1}]$ with width $\Delta_i=v_{i+1}-v_i$, a function H can now be written in terms of the base functions: $H=\sum_j H_jG_j$ in which by identification

$$(H_1,H_2,H_3,H_4)=\left(H(v_i),H(v_{i+1}),\Delta_i\frac{\mathrm{d}H}{\mathrm{d}v}(v_i),\Delta_i\frac{\mathrm{d}H}{\mathrm{d}v}(v_{i+1})\right). \qquad \text{(A2)}$$

Note that the local values for the base function derivatives contain the width of the interval. Adopting the distribution and its derivatives as independent variables allows for the use of non-uniform grids. At grid points where the grid density changes, the continuity of the dependent variables is ensured by appropriately adapting the Δs.

For a sufficiently dense grid, the variation of the coefficients is negligible with respect to that of the base functions (this can be upgraded by also taking that variation into account via the same polynomial expansion) and the equation becomes

$$\sum_j\left[\left[\frac{A(v)}{\Delta v}\right]\left[\int \mathrm{d}\xi\frac{\partial G_i}{\partial\xi}\frac{\partial G_j}{\partial\xi}\right]+[B(v)]\left[\int \mathrm{d}\xi\frac{\partial G_i}{\partial\xi}G_j\right]-[\Delta vC]\left[\int \mathrm{d}\xi G_iG_j\right]\right]F_{o,j}$$
$$\approx+\sum_j\left[[\Delta vv^2]\left[\int \mathrm{d}\xi G_iG_j\right]\right]S_j \qquad \text{(A3)}$$

where

$$(F_{o,1},F_{o,2},F_{o,3},F_{o,4})=\left(F_o(v_i),F_o(v_{i+1}),\Delta_i\frac{\mathrm{d}F_o}{\mathrm{d}v}(v_i),\Delta_i\frac{\mathrm{d}F_o}{\mathrm{d}v}(v_{i+1})\right) \qquad \text{(A4)}$$

and likewise for the source term S, so that three sets of integrals have to be evaluated once and for all: $\bar{\bar{I}}_0=\int \mathrm{d}\xi G_iG_j$, $\bar{\bar{I}}_1=\int \mathrm{d}\xi(\partial G_i/\partial\xi)G_j$, $\bar{\bar{I}}_2=\int \mathrm{d}\xi(\partial G_i/\partial\xi)(\partial G_j/\partial\xi)$.

https://doi.org/10.1017/S0022377821000234 Published online by Cambridge University Press

Ordering the values of the distribution at grid points in a vector, followed by a vector of the derivatives yields a block-diagonal linear system that can be solved with standard matrix inversion techniques.

As the Fokker–Planck equation is an equation of second order, two boundary conditions are required when solving it. At $v = 0$, neither the value of the distribution nor its derivative are *a priori* known but as no particles should escape across $v = 0$ imposing a vanishing flux $A\partial F_o/\mathrm{d}v + BF_o$ there seems to be a reasonable boundary condition. At infinity there are no particles, so either imposing $F_o = 0$ at the largest v seems natural. Alternatively, imposing the flux to be zero is equally suitable.

The fact that there is no need to adopt a uniform grid for the above described formalism is particularly handy as grid point regions can be made more or less dense according to the needs. In practice, there are a few regions where a higher grid point density is desirable: the thermal region (up to a few thermal velocities) and the region around the source. In absence of a local source term or strong collisional interaction, the grid can be somewhat relaxed. Since the zeros of the RF diffusion coefficients constitute a barrier for the particles, the distribution function typically drops to significantly lower values at these points. To ensure an as high as possible grid density in every region, it makes sense to monitor the location of the zeros and impose the maximally adopted velocity on it. Unless the RF power density is very high there is no need to have grid points beyond the first few zeros of $D_{vv,RF}$. In practice, typically 20 %–30 % of the grid points cover the thermal region and a similar amount the region around the source. The rest of the points are divided between the region in-between the thermal and source region, the region where RF acceleration of beam particles dominantly occur and the very high-energy region where the particle density is extremely low.

Appendix B. The influence matrix method

The influence matrix method (Ronquist & Patera 1987) is somewhat related to the finite element technique but exploiting it in mildly modified form (Van Eester *et al.* 2016*a*) allows us to avoid the need for inversion of a large matrix. The time it takes to solve a linear system crudely scales with the number of operations needed to invert the associated system matrix. The method suggested by Stix (only useful for solving the simplified Fokker–Planck equation in absence of a source) does not require inverting a large system matrix at all and is therefore extremely fast. The time needed to solve the equation using his method scales with the number N of unknown F_o values, i.e. grid points. Brute row elimination (Gauss–Jordan) inversion of a full matrix requires of order N^3 operations while exploiting the sparseness of the matrix to only do the necessary operations (no summing or multiplying by zero) provides substantial gain. If the system consists of similar blocks, the factorisation now requires only a number of operations of order $N^2 \log N$. The influence matrix method cleverly pushes down the number of the local unknowns by expressing them in terms of the remaining local ones, hereby effectively reducing the relevant N. Avoiding the need to invert the large matrix altogether is still faster, though. This is what the version of the influence matrix proposed here envisages: the scaling is brought back to linear but has a larger amount of computation to be done at each element. The method can be applied to any differential equation but – in view of its intended application for Fokker–Planck modelling – is demonstrated here for a second-order differential equation.

We start from a generic equation of the form

$$C_2(x)\frac{\mathrm{d}^2 Y}{\mathrm{d}x^2} + C_1(x)\frac{\mathrm{d}Y}{\mathrm{d}x} + C_0(x)Y + S(x) = 0. \tag{B1}$$

https://doi.org/10.1017/S0022377821000234 Published online by Cambridge University Press

The first step is a renormalisation of the independent variable to a reference scale, i.e. going from the variable x to the variable $\tilde{x} = x/x_{\text{ref}}$ where x_{ref} is of the same dimension as x and allows the dimensionless variable $\tilde{x}$ to be of order unity. In the context of Fokker–Planck solving, x is to be identified with the velocity v and one often exploits the dimensionless v/v_{th} rather than v as variable; v_{th} is the thermal velocity of the thermalised part of the test specie population. A second step is a renormalisation of the dependent variable. In the context of the present work this is useful since the distribution function varies over many orders of magnitude between the thermal region and that of the fast subpopulation. Although tiny, the distribution in the high-energy region is crucial: when computing the energy density, F_o is multiplied by the fourth power of the velocity, a function that is huge in the fast particle region compared with the values it assumes in the thermal region. As a consequence $v^4 F_o$ is typically of similar amplitude in both regions. To allow a sufficiently accurate representation of the solution Y in the whole region of interest, it is useful to derive an equation for a weighted dependent variable G rather than for the dependent variable Y itself. Introducing the notation $G(\tilde{x}) = H(\tilde{x})Y(\tilde{x})$ in which H is a suitable 'weight' function, once can easy find the equation G has to satisfy

$$\tilde{C}_2 \frac{\mathrm{d}^2 G}{\mathrm{d}\tilde{x}^2} + \tilde{C}_1 \frac{\mathrm{d}G}{\mathrm{d}\tilde{x}} + \tilde{C}_0 Y + \tilde{S} = 0 \tag{B2}$$

in which $\tilde{C}_2 = C_2\gamma(3,3)/x_{\text{ref}}^2$, $\tilde{C}_1 = C_2\gamma(3,2)/x_{\text{ref}}^2 + C_1\gamma(2,2)/x_{\text{ref}}$, $\tilde{C}_0 = C_2\gamma(3,1)/x_{\text{ref}}^2 + C_1\gamma(2,1)/x_{\text{ref}} + C_0\gamma(1,1)$ and $\tilde{S} = S$ and where $\bar{\bar{\gamma}}$ is the matrix connecting G, $dG/d\tilde{x}$ and $\mathrm{d}^2G/\mathrm{d}\tilde{x}^2$ to Y, $\mathrm{d}Y/\mathrm{d}\tilde{x}$ and $\mathrm{d}^2Y/\mathrm{d}\tilde{x}^2$:

$$\begin{pmatrix} G \\ G' \\ G'' \end{pmatrix} = \begin{pmatrix} H & 0 & 0 \\ H' & H & 0 \\ H'' & 2H' & H \end{pmatrix} . \begin{pmatrix} Y \\ Y' \\ Y'' \end{pmatrix} = \bar{\bar{\gamma}}^{-1} . \begin{pmatrix} Y \\ Y' \\ Y'' \end{pmatrix} \tag{B3}$$

where the notation $' = \mathrm{d}/\mathrm{d}\tilde{x}$ was introduced; the matrix $\bar{\bar{\gamma}}$ is readily obtained. The above differential equation is the actual starting point for adopting the influence matrix method. After subdividing the integration domain into a number N of small subintervals, the solution G_i in the ith subinterval is written as a polynomial $G_i \approx \sum_{m=0}^{n} G_{m,i}(\tilde{x} - \tilde{x}_{\text{ref}})^m$. The degree of the polynomial can be chosen freely depending on the need for accuracy and the subintervals do not need to be uniformly spaced, so regions where enhanced attention is required can be given a finer gridding. As is done for the more usual finite element representation, the local approximation is chosen here to be a polynomial of third order ($n = 3$), i.e. imposing four degrees of freedom, two to be associated with the unknown and its derivative at the left-hand edge of the interval, and two at the right-hand edge. Inserting the local polynomial approximation in the equation and demanding it is satisfied at both ends of the interval yields two equations connecting two of the local coefficients to the other two:

$$\bar{\bar{N}}_i . \begin{pmatrix} G_{0,i} \\ G_{1,i} \end{pmatrix} + \bar{\bar{M}}_i . \begin{pmatrix} G_{2,i} \\ G_{3,i} \end{pmatrix} + \begin{pmatrix} \tilde{S}(\tilde{x}_i) \\ \tilde{S}(\tilde{x}_{i+1}) \end{pmatrix} = \begin{pmatrix} 0 \\ 0 \end{pmatrix} . \tag{B4}$$

Here

$$\bar{\bar{N}}_i = \begin{pmatrix} \tilde{C}_0(\tilde{x}_i) & \tilde{C}_1(\tilde{x}_i) \\ \tilde{C}_0(\tilde{x}_{i+1}) & \tilde{C}_1(\tilde{x}_{i+1}) + \tilde{C}_0(\tilde{x}_{i+1})\Delta_i \end{pmatrix} \tag{B5}$$

https://doi.org/10.1017/S0022377821000234 Published online by Cambridge University Press

and

$$\bar{\bar{M}}_i = \begin{pmatrix} 2\tilde{C}_2(\tilde{x}_i) & 0 \\ 2\tilde{C}_2(\tilde{x}_{i+1}) + 2\tilde{C}_1(\tilde{x}_{i+1})\Delta_i + \tilde{C}_0(\tilde{x}_{i+1})\Delta_i^2 & 6\tilde{C}_2(\tilde{x}_{i+1})\Delta_i + 3\tilde{C}_1(\tilde{x}_{i+1})\Delta_i^2 + \tilde{C}_0(\tilde{x}_{i+1})\Delta_i^3 \end{pmatrix}. \tag{B6}$$

Here $\Delta_i = \tilde{x}_{i+1} - \tilde{x}_i$. Two of the four unknowns to be expressed in terms of the other two, the number of unknowns to be found when solving the global system has hereby been halved. The remaining ones are determined by imposing that G and its derivative are continuous at the interfaces between neighbouring elements, and – at either end of the full integration interval – by imposing the boundary conditions. At an internal boundary the continuity can be expressed in the form of a 2×2 linear system,

$$\bar{\bar{R}}_i . \begin{pmatrix} G_{0,i} \\ G_{1,i} \end{pmatrix} - \begin{pmatrix} \tilde{\tilde{S}}_{i,1} \\ \tilde{\tilde{S}}_{i,2} \end{pmatrix} = \begin{pmatrix} G_{0,i+1} \\ G_{1,i+1} \end{pmatrix} \tag{B7}$$

in which

$$\bar{\bar{R}}_i = \bar{\bar{P}}_i - \bar{\bar{Q}}_i . \bar{\bar{M}}_i^{-1} . \bar{\bar{N}}_i, \tag{B8}$$

$$\begin{pmatrix} \tilde{\tilde{S}}_{i,1} \\ \tilde{\tilde{S}}_{i,2} \end{pmatrix} = \bar{\bar{Q}}_i . \bar{\bar{M}}_i^{-1} . \begin{pmatrix} \tilde{S}(\tilde{x}_i) \\ \tilde{S}(\tilde{x}_{i+1}) \end{pmatrix}, \tag{B9}$$

$$(\bar{\bar{P}}_i = \begin{pmatrix} 1 & \Delta_i \\ 0 & 1 \end{pmatrix}, \tag{B10}$$

$$\bar{\bar{Q}}_i = \begin{pmatrix} \Delta_i^2 & \Delta_i^3 \\ 2\Delta_i^2 & 3\Delta_i^2 \end{pmatrix}. \tag{B11}$$

Via the above, a solution can be propagated from one element to the next. This yields two equations for the four unknowns $G_{0,1}$, $G_{1,1}$, $G_{0,N}$ and $G_{1,N}$ at the extremities of the integration interval. To uniquely find the solution to the differential equation, two more equations are required. The two boundary conditions are exactly what is needed. For the second-order equation at hand the boundary conditions are of the general form $\alpha_{\rm BC} {\rm d}Y/{\rm d}x + \beta_{\rm BC} Y = \gamma_B C$. Transformed to $\tilde{x}$ and G these conditions are of the form

$$\tilde{\alpha}_{\rm BC} \frac{{\rm d}G}{{\rm d}\tilde{x}} + \tilde{\beta}_{\rm BC} G = \tilde{\gamma}_{\rm BC} \tag{B12}$$

with $\tilde{\alpha}_{\rm BC} = \alpha_{\rm BC}\gamma(2,2)/x_{\rm ref}$, $\tilde{\beta}_{\rm BC} = \alpha_{\rm BC}\gamma(2,1)/x_{\rm ref} + \beta_{\rm BC}\gamma(1,1)$ and $\tilde{\gamma}_{\rm BC} = \gamma_{\rm BC}$.

This system of four linear equation can be solved to find the four required quantities. Once these are obtained the full solution can be reconstructed by using the local system connecting neighbouring elements.

REFERENCES

BILATO, R., BRAMBILLA, M., MAJ, O., HORTON, L. D., MAGGI, C. F. & STOBER, J. 2011 Simulations of combined neutral beam injection and ion cyclotron heating with the TORIC-SSFPQL package. *Nucl. Fusion* **51**, 103034.

BOSCH, H.S. & HALE, G.M. 1992 Improved formulas for fusion cross-sections and thermal reactivities. *Nucl. Fusion* **32**, 611.

BRAMBILLA, M. 1994 Quasi-linear ion distribution function during ion cyclotron heating in tokamaks. *Nucl. Fusion* **34**, 1121.

https://doi.org/10.1017/S0022377821000234 Published online by Cambridge University Press

BREZINSEK, S., *et al.* 2013 Fuel retention studies with the ITER-Like Wall in JET. *Nucl. Fusion* **53**, 083023.

COSTER, D., BASIUK, V., PEREVERZEV, G., KALUPIN, D., ZAGORSKI, R., STANKIEWICZ, R., HUYNH, P. & IMBEAUX, F. 2010 The European transport solver. *IEEE Trans. Plasma Sci*. **38** (9), 2085.

FALCHETTO, G. L., COSTER, D., COELHO, R., SCOTT, B. D., FIGINI, L., KALUPIN, D., NARDON, E., NOWAK, S., ALVES, L. L., ARTAUD, J.-F., *et al.* 2014 The European Integrated Tokamak Modelling (ITM) effort: achievements and first physics results. *Nucl. Fusion* **54**, 043018.

FALCHETTO, G. L., AIRILA, M. I., ALBERTO, M. A., ANDERSSON, S. E., ANIEL, T., ARTAUD, J.-F., ASUNTA, O., ATANASIU, C. V., BAELMANS, M., BASIUK, V., *et al.* 2016 EUROfusion Integrated Modelling (EU-IM) capabilities and selected physics applications. In *26th IAEA Fusion Energy Conference*.

FALCHETTO, G.L., *et al.* 2019 Multi-machine analysis of EU experiments using the EUROfusion Integrated Modelling (EU-IM) framework. In *Proceedings of the 46th Conference on Plasma Physics*.

GAFFEY, J.D. 1976 Energetic ion distribution resulting from neutral beam injection in tokamaks. *J. Plasma Phys*. **16**, 149.

GARZOTTI, L., CHALLIS, C., DUMONT, R., FRIGIONE, D., GRAVES, J., LERCHE, E., MAILLOUX, J., MANTSINEN, M., RIMINI, F., CASSON, F., *et al.* 2019 Scenario development for D-T operation at JET. *Nucl. Fusion* **59**, 076037.

GONICHE, M., LERCHE, E., JACQUET, P., VAN EESTER, D., BOBKOV, V., BREZINSEK, S., COLAS, L., CZARNECKA, A., DREWELOW, P., DUMONT, R., *et al.* 2014 Optimization of ICRH for tungsten control in JET H-mode plasmas. In *Proceedings of the 41th EPS on Conference on Controlled Fusion and Plasma Physics*, vol. 45.

HARVEY, R. W., MCCOY, M. G., KERBEL, G. D. & CHIU, S. C. 1986 ICRF fusion reactivity enhancement in tokamaks. *Nucl. Fusion* **26**, 43.

HARVEY, R. W. & MCCOY, M. G. 1992 The CQL3D code. In *Proceedings of the IAEA TCM on Advances in Simulation and Modeling of Thermonuclear Plasmas*, vol. 489.

HAWRYLUK, R. J. 1980 An empirical approach to tokamak transport. In *Physics of Plasmas Close to Thermonuclear Conditions* (ed. B. Coppi et al.), vol. 1, p. 19.

HEDIN, J., HELLSTEN, T., ERIKSSON, L.-G. & JOHNSON, T. 2002 The influence of finite drift orbit width on ICRF heating in toroidal plasmas. *Nucl. Fusion* **42** (5), 527.

HIRVIJOKI, E., ASUNTA, O., KOSKELA, T., KURKI-SUONIO, T., MIETTUNEN, J., SIPILÄ, S., SNICKER, A. & ÄKÄSLOMPOLO, A. 2014 ASCOT: solving the kinetic equation of minority particle species in tokamak plasmas. *Comput. Phys. Commun*. **185** (4), 1310.

HUYNH, P., LERCHE, E. A., VAN EESTER, D., BILATO, R., VARJE, J., JOHNSON, T., SAUTER, O., VILLARD, L., FERREIRA, J. & JET CONTRIBUTORS AND THE EUROFUSION-IM TEAM 2019 Modeling ICRH and ICRH-NBI synergy in high power JET scenarios using European Transport Simulator (ETS). In *Proceedings of the 23rd Topical Conference on RF Power in Plasmas*.

HUYNH, P., LERCHE, E., VAN EESTER, D., GARCIA, J., JOHNSON, T., FERREIRA, J., KIROV, K., YADYKIN, D., & STRAND, P. 2020 European transport simulator modelling: the role of ICRH/NBI synergy in the extrapolation of high power JET D scenarios to D-T, submitted to Nuclear Fusion.

IMBEAUX, F., LISTER, J. B., HUYSMANS, G. T. A., ZWINGMANN, W., AIRAJ, M., APPEL, L., BASIUK, V., COSTER, D., ERIKSSON, L. G., GUILLERMINET, B., *et al.* 2010 A generic data structure for integrated modelling of tokamak physics and subsystems. *Comput. Phys. Commun*. **181**, 987.

IMBEAUX, F., PINCHES, S. D., LISTER, J. B., BURAVAND, Y., CASPER, T., DUVAL, B., GUILLERMINET, B., HOSOKAWA, M., HOULBERG, W., HUYNH, P., *et al.* 2015 Design and first applications of the ITER integrated modelling & analysis suite. *Nucl. Fusion* **55** (12), 123006.

JACQUINOT, J., BHATNAGAR, V. P., CORDEY, J. G., HORTON, L. D., START, D. F. H., BARNSLEY, R., BREGER, P., CHRISTIANSEN, J. P., CLEMENT, S., DAVIES, S. J., *et al.* 1999 Overview of ITER physics deuterium-tritium experiments in JET. *Nucl. Fusion* **39**, 235.

https://doi.org/10.1017/S0022377821000234 Published online by Cambridge University Press

JAEGER, E. F., BERRY, L. A., AHERN, S. D., BARRETT, R. F., BATCHELOR, D. B., CARTER, M. D., D'AZEVEDO, E. F., MOORE, R. D., HARVEY, R. W., MYRA, J. R., *et al.* 2006 Self-consistent full-wave and Fokker-Planck calculations for ion cyclotron heating in non-Maxwellian plasmas. *Phys. Plasmas* **13**, 056101.

JOFFRIN, E., SIPS, A. C. C., ARTAUD, J. F., BECOULET, A., BERTALOT, L., BUDNY, R., BURATTI, P., BELO, P., CHALLIS, C. D., CRISANTI, F., *et al.* 2005 The 'hybrid' scenario in JET: towards its validation for ITER. *Nucl. Fusion* **45**, 626.

JOFFRIN, E., BARUZZO, M., BEURSKENS, M., BOURDELLE, C., BREZINSEK, S., BUCALOSSI, J., BURATTI, P., CALABRO, G., CHALLIS, C. D., CLEVER, M., *et al.* 2014 First scenario development with the JET new ITER-like wall. *Nucl. Fusion* **54**, 013011.

JOFFRIN, E., ABDUALLEV, S., ABHANGI, M., ABREU, P., AFANASEV, V., AFZAL, M., AGGARWAL, K. M., AHLGREN, T., AHO-MANTILA, L., AIBA, N., *et al.* 2019 Overview of the JET preparation for deuterium-tritium operation with the ITER like-wall. *Nucl. Fusion* **59**, 112021.

JOLY, J., GARCIA, J., IMBEAUX, F., DUMONT, R., SCHNEIDER, M., JOHNSON, T. & ARTAUD, J.-F. 2019 Self-consistent modelling of heating synergy between NBI and ICRH in JET deuterium plasmas. *Plasma Phys. Control. Fusion* **61**, 075017.

JUCKER, M. 2010 Self-consistent ICRH distribution functions and equilibria in magnetically confined plasmas. PhD thesis, CRPP/EPFL, Lausanne, Switzerland.

KALUPIN, D., BASIUK, V., COSTER, D., HUYNH, P. H., ALVES, L. L., ANIEL, T. H., ARTAUD, J.-F., BIZARRO, J. P. S., BOULBE, C., COELHO, R., *et al.* 2012 The European transport solver: an integrated approach for transport simulations in the plasma core. In *24th IAEA Fusion Energy Conference*.

KARNEY, C.F. F 1986 Fokker-Planck and quasilinear codes. *Comput. Phys. Rep*. **4**, 183.

KEILHACKER, M., GIBSON, A., GORMEZANO, C., LOMAS, P. J., THOMAS, P. R., WATKINS, M. L., ANDREW, P., BALET, D., BORBA, D., CHALLIS, C. D., *et al.* 1999 High fusion performance from deuterium-tritium plasmas in JET. *Nucl. Fusion* **39**, 209.

KIM, H.-T., SIPS, A. C. C., ROMANELLI, M., CHALLIS, C. D., RIMINI, F., GARZOTTI, L., LERCHE, E., BUCHANAN, J., YUAN, X., KAYE, S. & JET CONTRIBUTORS 2018 High fusion performance at high T_i/T_e in JET-ILW baseline plasmas with high NBI heating power and low gas puffing. *Nucl. Fusion* **58**, 036020.

LAMALLE, P.U. 1994 Nonlocal theoretical generalization and tridimensional study of the coupling of an ICRH antenna to a tokamak plasma. PhD Thesis, LPP-ERM/KMS Rep. 101, Université de Mons, Mons, Belgium.

LEE, J., WRIGHT, J., BERTELLI, N., SMITHE, D., VALEO, E., PETROV, Y., JAEGER, E. F., BERRY, L., HARVEY, R. & BONOLI, P. 2017 A new quasilinear formulation for ICRF plasmas in a toroidal geometry. *Eur. Phys. J*. **157**, 03028.

LERCHE, E., VAN EESTER, D., KRASILNIKOV, A., ONGENA, J., LAMALLE, P. & JET-EFDA CONTRIBUTORS 2009 Modelling of D majority ICRH at JET: impact of absorption at the Doppler-shifted resonance. *Plasma Phys. Control. Fusion* **51**, 044006.

LERCHE, E., GONICHE, M., JACQUET, P., VAN EESTER, D., BOBKOV, V., COLAS, L., MONAKHOV, I., RIMINI, F., CZARNECKA, A., CROMBÉ, K., *et al.* 2015 ICRH for core impurity mitigation in JET-ILW. *AIP. Conf. Proc*. **1689**, 030002.

LERCHE, E., LENNHOLM, M., CARVALHO, I. S., DUMORTIER, P., DURODIE, F., VAN EESTER, D., GRAVES, J., JACQUET, P. H., MURARI, A. & JET CONTRIBUTORS 2017 Sawtooth pacing with on-axis ICRH modulation in JET-ILW. *Nucl. Fusion* **57**, 036027.

LITAUDON, X., ABDUALLEV, S., ABHANGI, M., ABREU, P., AFZAL, M., AGGARWAL, K. M., AHLGREN, T., AHN, J. H., AHO-MANTILA, L., AIBA, N., *et al.* 2017 Overview of the JET results in support to ITER. *Nucl. Fusion* **57**, 102001.

PETROV, Y.V. & HARVEY, R.W. 2016 A fully-neoclassical finite-orbit-width version of the CQL3D Fokker-Planck code. *Plasma Phys. Control. Fusion* **58**, 115001.

PHILIPPS, V., MERTENS, P. H., MATTHEWS, G. F., MAIER, H. & JET-EFDA CONTRIBUTORS 2010 Overview of the JET ITER-like Wall Project. *Fusion Engng Des*. **85**, 1581.

https://doi.org/10.1017/S0022377821000234 Published online by Cambridge University Press

PINCHES, S. D., ARTAUD, J. F., CASSON, F. J., CORRIGAN, G., DE BOCK, M., DUBROV, M., HARYING, D., HOLLOCOMBE, J., HOSOKAWA, M., IMBEAUX, F., *et al.* 2018 Progress in the ITER integrated modelling programme and the ITER scenario database. In *27th IAEA Fusion Energy Conference - IAEA CN-258*.

PINCHES, S. D., AKERS, R., ANDRE, R., ANIEL, T., BANDYOPADHYAY, I., BASIUK, V., BELLI, E. A., BONNIN, X., CANDY, J., CHATTOPADHYAY, A. K., *et al.* 2016 Progress in the ITER integrated modelling programme and the use and validation of IMAS within the ITER Members. In *Proceedings of the 26th IAEA Fusion Energy Conference*.

ROMANELLI, M. & EUROFUSION WPCD TEAM 2019 Status of code integration, verification and validation in EUROfusion. In *3rd IAEA Technical Meeting on Fusion Data Processing, Validation and Analysis*.

ROMANELLI, M., *et al.* 2020 Predictive multi-physics integrated modelling of tokamaks scenarios using the ITER Integrated Modelling and Analysis System (IMAS) in support of ITER Exploitation. In *28th IAEA Fusion Energy Conference*, postponed to 2021 (Covid).

RONQUIST, E.M. & PATERA, A.T. 1987 Spectral element multigrid. I. Formulation and numerical results. *J. Sci. Comput*. **2**, 389.

SCHNEIDER, M., JOHNSON, T., DUMONT, R., ERIKSSON, J., ERIKSSON, L.-G., GIACOMELLI, L., GIRARDO, J. B., HELLSTEN, T., KHILKEVITCH, E., KIPTILY, V. G., *et al.* 2016 Modelling third harmonic ion cyclotron acceleration of deuterium beams for JET fusion product studies experiments. *Nucl. Fusion* **56**, 112022.

SCHNEIDER, M., ARTAUD, J.-F., BONOLI, P., KAZAKOV, Y., LAMALLE, P. H., LERCHE, E., VAN EESTER, D. & WRIGHT, J. 2017 ICRF heating schemes for the ITER non-active phase. *Eur. Phys. J*. **157**, 03046.

SCHNEIDER, M., POLEVOI, A. R., KIM, S. H., LOARTE, A., PINCHES, S. D., ARTAUD, J.-F., MILITELLO-ASP, E., BEAUMONT, B., BILATO, R., BOILSON, D., *et al.* 2019 Modelling one-third field operation in the ITER pre-fusion power operation phase. *Nucl. Fusion* **59**, 126014.

SCHNEIDER, M., MITTERAUER, V., PINCHES, S., JOHNSON, T., ARBINA, I., ARTAUD, J.-F., VAN EESTER, D., FIGINI, L., KOJIMA, S., LERCHE, E., *et al.* 2020 Simulation of heating and current drive sources for various scenarios of the ITER research plan. In *62nd Annual Meeting on the APS Division of Plasma Physics*.

START, D. F. H., JACQUINOT, J., BERGEAUD, V., BHATNAGAR, V. P., CONROY, S. W., COTTRELL, G. A., CLEMENT, S., ERICSSON, G., ERIKSSON, L.-G., FASOLI, A., *et al.* 1999 Bulk ion heating with ICRH in JET DT plasmas. *Nucl. Fusion* **39**, 321.

STIX, T. H. 1992 *Waves in Plasmas*. AIP.

STRAND, P., COELHO, R., COSTER, D., ERIKSSON, L.-G., IMBEAUX, F., GUILLERMINET, B., CONTRIBUTORS TO THE EFDA ITM-TF WORK PROGRAMME & THE EUFORIA PROJECT 2010 Simulation and high performance computing - building a predictive capability for fusion. *Fusion Engng Des*. **85**, 383.

STRAND, P., SEE, Y., FERREIRA, J., FIGUEIREDO, A., COELHO, R., LERCHE, E.,VAN EESTER, D., MORADI, S., JOHNSON, T., THOLERUS, E., *et al*. 2018 Towards a predictive modelling capacity for DT plasmas: European Transport Simulator (ETS) verification and validation. IAEA CN-258, Gandhinagar, India, TH/P6-14.

THE KEPLER PROJECT 2008 https://kepler-project.org/users/documentation.html.

VAN EESTER, D. 2001 Evaluating the efficiency of radiofrequency heating in tokamaks: the impact of orbital topology and poloidal inhomogeneity. *J. Plasma Phys*. **65**, 407.

VAN EESTER, D. & LERCHE, E.A. 2011 Simple 1D Fokker-Planck modelling of ion cyclotron resonance frequency heating at arbitrary cyclotron harmonics accounting for Coulomb relaxation on non-Maxwellian populations. *Plasma Phys. Control. Fusion* **53**, 092001.

VAN EESTER, D., CROMBÉ, K., LAUWENS, B., KAZAKOV, Y., VERGOTE, M. & VAN SCHOOR, M. 2016*a* A new tool for modelling ion cyclotron resonance heating wave propagation and damping in non-axisymmetrical magnetic confinement fusion machines. In *Proceedings of the 43rd EPS Conference on Plasma Physics*.

https://doi.org/10.1017/S0022377821000234 Published online by Cambridge University Press

Van Eester, D., Lerche, E., Kazakov, Y., Jacquet, P., Bobkov, V., Crombé, K., Czarnecka, A., Dumont, R., Eriksson, J., Giacomelli, L., *et al.* 2016*b* Recent ion cyclotron resonance heating experiments in JET in preparation of a DT campaign. In *26th IAEA Fusion Energy Conference*.

Voitsekhovitch, I., Hatzky, R., Coster, D., Imbeaux, F., Mc Donald, D. C., Fehér, T. B., Kang, K. S., Leggate, H., Martone, M., Mochalskyy, S., *et al.* 2018 Recent EUROfusion achievements in support of computationally demanding multiscale fusion physics simulations and integrated modeling. *Fusion Sci. Technol*. **74**, 186.

https://doi.org/10.1017/S0022377821000234 Published online by Cambridge University Press